

Hot, Retrograde Tilted MADs: Misaligned, Precessing, and Shaped by Electromagnetic Torques

SAJAL GUPTA ¹ AND JASON DEXTER  ¹

¹ *JILA and Department of Astrophysical and Planetary Sciences, University of Colorado, Boulder, CO 80309, USA*

Submitted to ApJ

ABSTRACT

Tilted accretion disks in the magnetically arrested (MAD) state may be present in X-ray binaries and active galactic nuclei such as Sgr A* and M87. We have carried out 3D global GRMHD simulations to study the evolution of these accretion flows as a function of black hole spin and misalignment angle. Prograde MADs align with the spin through a two-stage process: an initial rapid alignment phase that operates on the magnetic flux saturation timescale, followed by a slower, spin-independent phase. In contrast, retrograde MADs remain persistently misaligned regardless of the black hole spin, displaying solid-body precession at rates four times higher than weakly magnetized flows at the same spin magnitude. By deriving torque equations in ideal GRMHD and evaluating them in a frame aligned with instantaneous disk orientation, we demonstrate that electromagnetic (EM) torques always act to align the disk with the BH spin, but are countered by opposing hydrodynamic fluxes in retrograde flows. We further develop a preliminary empirical model to explain the cause of two-stage prograde alignment and discuss the possibility of alignment in the retrograde MAD. Strongly magnetized, retrograde, misaligned accretion disks provide a candidate scenario for the low-frequency quasi-periodic oscillations in black hole X-ray binaries.

1. INTRODUCTION

The angular momentum of a black hole (BH) is largely shaped by its history of interactions—from mergers with other massive BHs and stars to accretion of surrounding gas (Bardeen 1970; King et al. 2005). Because of these dynamic processes, the inflowing plasma and its magnetic field can often be misaligned with the BH’s spin axis. In many astrophysical settings, external torques naturally induce such tilts: tidal interactions in X-ray binaries (XRBs; Katz 1980; Larwood 1998; Wijers & Pringle 1999), radiation pressure (Pringle 1997), and stellar winds—including those from Wolf–Rayet stars near Sgr A* (Schandl & Meyer 1994; Ghez et al. 1998; Genzel et al. 2010)—can all misalign the accretion flow relative to the BH spin axis.

While the Bardeen-Petterson effect (Bardeen & Petterson 1975) is often invoked to suggest that the inner parts of the accretion disk and BH spin should achieve mutual alignment, both numerical (Nelson & Papaloizou 2000; Liska et al. 2019; Raj et al. 2021) and analytical

studies (Nixon & King 2012; Nixon et al. 2013) show that this effect is primarily effective for thin, viscous disks with relatively small tilt angles. Thicker disks, however, tend to warp further away from alignment (Papaloizou & Lin 1995; Ivanov & Illarionov 1997; Lubow et al. 2002). For instance, hot, weakly magnetized accretion flows—such as those likely feeding Sgr A* (Yuan et al. 2003; Collaboration et al. 2022)—and systems undergoing super-Eddington accretion (Abramowicz et al. 1980; Jiang et al. 2019). In such systems, alignment with the BH spin remains partial at best, with only the inner disk showing a weak tendency to align (Fragile et al. 2007; White et al. 2019; Gupta & Dexter 2024).

However, alignment dynamics differ significantly in magnetically arrested disks (MADs; Narayan et al. 2003; Igumenshchev et al. 2003). Such flows are likely prevalent in systems like M87 (Collaboration et al. 2021; Yuan et al. 2022), certain XRBs (You et al. 2023), and active galactic nuclei (McKinney et al. 2012). In MAD configurations, the accretion flow carries a large amount of coherent poloidal magnetic flux that accumulates and saturates near the BH (Igumenshchev 2008; Begelman et al. 2022), leading to a formation of a relativistic jet

(Blandford & Znajek 1977; Blandford & Payne 1982; Tchekhovskoy et al. 2011; Narayan et al. 2012).

McKinney et al. (2013) suggested that in tilted MADs, this relativistic jet exerts an asymmetric force on the disk (Polko & McKinney 2016), promoting alignment with the BH spin even for fast-spinning BHs undergoing extreme misalignment ($\sim 90^\circ$). They coined the term ‘magneto-spin alignment’ to describe this mechanism, and suggested that it may operate for moderately rotating BHs, with spin as low as $a \gtrsim 0.2$ for thick MADs and $a \gtrsim 0.5$ for thinner ones. However, questions remain about how the jet can exert the torque needed for alignment, as modeled by Polko & McKinney (2016), if it is emitted perpendicular to the average disk plane. As for the jet to drive alignment, it must push on the disk asymmetrically, implying that it cannot be strictly perpendicular. Yet, recent simulations by Liska et al. (2018); Chatterjee et al. (2020) indicate that jets from strongly magnetized flows may indeed align closely with the disk’s angular momentum vector, potentially challenging this proposed alignment mechanism.

These contrasting findings raise fundamental questions about the physical processes underlying disk alignment in MADs. Additionally, Chatterjee et al. (2025) studied hot, tilted MADs and found that retrograde disks, in contrast to McKinney et al. (2013)’s results, do not align with the BH axis of symmetry. This discrepancy suggests two pressing questions: why do retrograde disks remain misaligned in these simulations, and what factors in McKinney et al. (2013) study led to alignment across a wide range of tilt angles?

In this paper, we argue that jets do, in fact, emit nearly along the disk’s rotational axis, and it is primarily the magnetic stresses—particularly the radial-polar magnetic tension—that drive alignment in prograde flows. The structure of this paper is as follows: In Section 2, we outline the governing equations and simulation setup for our ideal, general relativistic magnetohydrodynamic (GRMHD) simulations. In section 3, we analyze the tilt profiles of both the jet and the disk, showing that while retrograde flows remain misaligned, prograde flows align in two distinct phases: a rapid phase that concludes once the magnetic flux threading the BH saturates, followed by a slower alignment phase, as illustrated in Figure 1. Section 4 examines the relative contributions of physical process in disk alignment, showing that magnetic torques generally act to reduce the disk–spin misalignment in both prograde and retrograde flows. An empirical scaling for the alignment torque and a two-stage picture of prograde evolution is described in section 4.3. Section 5 showcases the near rigid-body precession of retrograde disks, and in sec-

tion 6, we address the alignment potential for retrograde flows and discuss the retrograde precession of prograde flows. Finally, Section 7 concludes our findings.

2. METHODS

2.1. Governing Equations

We use the publicly available HARMPI code (Tchekhovskoy 2019) (a parallel, 3D version of HARM (Gammie et al. 2003; Noble et al. 2006)) to solve the idealized GRMHD equations of motion written in the following form:

$$\partial_t (\sqrt{-g} \rho u^t) + \partial_j (\sqrt{-g} \rho u^j) = 0, \quad (1)$$

$$\partial_t (\sqrt{-g} T_\mu^t) + \partial_j (\sqrt{-g} T_\mu^j) - \sqrt{-g} T_\lambda^\kappa \Gamma_{\mu\kappa}^\lambda = 0, \quad (2)$$

$$\nabla_\nu (*F^{\mu\nu}) = 0, \quad (3)$$

where ρ is the fluid frame density, u^μ is the contravariant 4-velocity, $g \equiv \det(g_{\mu\nu})$ is the metric determinant, and $\Gamma_{\mu\kappa}^\lambda$ are the connection coefficients. The Greek alphabets are used to represent four-vector, whereas Latin alphabets describe spatial components. We describe the space-time of rotating BH using spherical polar Kerr-Schild coordinates (Font et al. 1998) with a metric signature $(-, +, +, +)$. Here, T_ν^μ and $*F^{\mu\nu}$ are the ideal MHD stress-energy tensor and dual electromagnetic tensor, respectively, defined as

$$T_\nu^\mu = (\rho h + b^2) u^\mu u_\nu + (p_{\text{gas}} + p_{\text{mag}}) \delta_\nu^\mu - b^\mu b_\nu, \quad (4)$$

$$*F^{\mu\nu} = b^\mu u^\nu - b^\nu u^\mu, \quad (5)$$

where p_{gas} is the gas pressure, $h = 1 + \gamma p_{\text{gas}}/(\rho(\gamma - 1))$ is the specific enthalpy, $\gamma = 5/3$ is the adiabatic index, b^μ is the contravariant fluid-frame magnetic 4-field, and $p_{\text{mag}} \equiv b^\mu b_\mu/2 = b^2/2$ is the magnetic pressure.

2.2. Simulation Setup

We simulate tilted MADs for seven BH spin values (a), ranging from $a = -0.9375$ to $a = 0.9375$. The models were run at two resolutions (five high-resolution and two low-resolution); see Table 1 for details. The dimensionless spin parameter a is defined as $-1 < a \equiv c\mathbf{L}_{\text{BH}}/GM_{\text{BH}}^2 < 1$, and \mathbf{L}_{BH} represents the angular momentum vector of a BH. Each simulation initializes an isentropic hydro-equilibrium torus (Fishbone & Moncrief 1976) with inner radius at $r_{\text{in}} = 12 r_g$, where $r_g \equiv GM_{\text{BH}}/c^2$ denotes one gravitational radii. For prograde spins ($a > 0$), the pressure maximum is fixed at $r_{\text{max}} = 25 r_g$. Whereas, for retrograde spins ($a < 0$), r_{max} is adjusted within $25 - 27 r_g$. This adjustment is made to keep the radial extent of the tori (specifically, the outer radius r_{out}) approximately similar across same

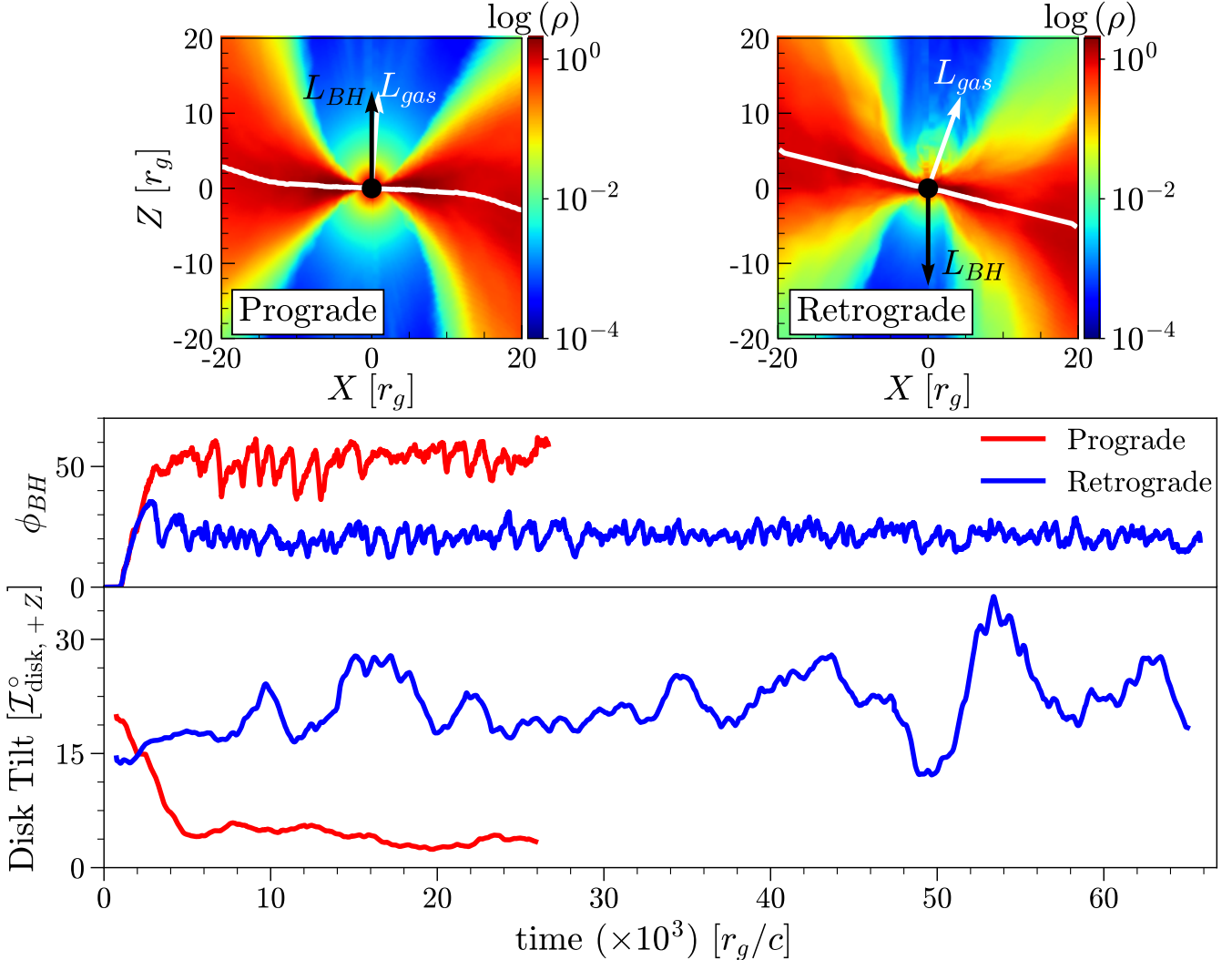


Figure 1. Top panel: Poloidal slice snapshots of density (ρ) for high-spin prograde ($a \approx 0.94$) and retrograde ($a \approx -0.94$) cases, captured during their respective flux saturation time. Both flows are initially tilted by 16° from the $+z$ axis (see equation 10). The white line denotes the averaged disk plane, and black and white arrows indicate the directions of the BH and disk angular momenta, respectively. **Middle panel:** Evolution of normalized magnetic flux threading the event horizon. **Bottom panel:** Disk tilt evolution from the event horizon to $20 r_g$. The figure demonstrates that prograde flows align with the BH spin axis, whereas retrograde flows remain misaligned. Here, for comparison to the prograde case, the tilt evolution for retrograde flow was shown relative to $+z$ -axis.

magnitudes of spin. Table 1 lists the inner radius and pressure maximum for each simulation.

The torus is then rotated about the BH's equatorial plane such that its initial angular momentum lies in the x - z plane. We initialize tilt angles of 16° and/or 30° in our simulations, allowing us to investigate the effect of the initial misalignment without the disk entering the polar region. A single poloidal magnetic field loop threads the torus, initialized to saturate magnetic flux on the BH, with the maximum plasma-beta parameter ($\beta = p_{\text{gas}}/p_{\text{mag}}$) of 100. To verify that key diagnostics (e.g. average disk inclination and magnetic-flux evolution) do not depend on whether one rotates the

disk or flips the BH spin axis, we carried out symmetry tests for a 16° misaligned disk around high-spin BHs ($a = \pm 0.9375$). These tests confirm identical results under the two equivalent initialization schemes and are described in Appendix C.

We evolve all simulations in modified spherical-polar Kerr-Schild coordinates (r, θ, ϕ) . Our primary set—comprising both prograde and high spin retrograde—uses a resolution of $320 \times 256 \times 160$ cells (see Table 1). To explore how spin and tilt trends might extend beyond this core grid, we additionally perform three lower-resolution retrograde test runs ($160 \times 128 \times 80$ cells) at $a = -0.1, -0.5$, and -0.9375 (the latter with a 30° tilt).

Table 1. List of the simulations presented in this work.

BH spin	$\mathcal{I}_{\text{disk,BH}}^{\circ}$ (t=0)	r_{max} [r_g]	Resolution $N_r \times N_\theta \times N_\phi$	t_{sim} [$10^3 r_g/c$]	$\langle \phi_{\text{BH}} \rangle$	t_{rapid} [$10^3 r_g/c$]	$\langle \mathcal{I}_{\text{disk,BH}}^{\circ} \rangle$ ($10 r_g$)	$\langle \mathcal{I}_{\text{jet}}^{\circ} \rangle$ ($10 r_g$)	Summary
Prograde MADs									
0.3	16°	25	$320 \times 256 \times 160$	52.7	59.3	0.65	9.1°	9.3°	Aligning
0.5	16°	25	$320 \times 256 \times 160$	51.7	59.6	0.625	7.4°	7.7°	Aligning
0.5	30°	25	$320 \times 256 \times 160$	29.2	61.7	0.625	12°	10.4°	Aligning
0.75	16°	25	$320 \times 256 \times 160$	25.2	59.3	0.59	6°	6.3°	Aligning
0.9375	16°	25	$320 \times 256 \times 160$	26.7	52.7	0.54	5°	6.1°	Aligned
Retrograde MADs									
-0.9375	164°	27.125	$320 \times 256 \times 160$	65.7	21.1	—	160.3°	163.2°	Persistently misaligned
Retrograde MADs (Lower resolution test runs)									
-0.1	150°	25.2	$160 \times 128 \times 80$	71.4	51.7	—	147.5°	150.8°	Persistently misaligned
-0.5	150°	26.1	$160 \times 128 \times 80$	34.1	33.9	—	148.2°	155.3°	Persistently misaligned
-0.9375	150°	27.125	$160 \times 128 \times 80$	80.5	20.4	—	150.1°	166.4°	Persistently misaligned

NOTE—The first column indicates the BH dimensionless spin, where positive/negative values correspond to BH orientation along the $\pm z$ -axis. The second column shows the initial tilt of the disk relative to the spin axis. The third, fourth, and fifth columns provide the location of the pressure maximum, resolution, and final simulation time, respectively. The sixth column presents the time-averaged MAD parameter. The seventh column marks the end of the rapid alignment phase in prograde flows, coinciding with the flux saturation timescale. The eighth and ninth columns report the evolved relative tilt between the BH spin axis and the disk and jet at $r = 10 r_g$, respectively. The final column summarizes the disk alignment status at $r = 10 r_g$: ‘aligning’ indicates ongoing alignment at the end of the simulation, while ‘aligned’ or ‘persistently misaligned’ indicates that the disk has reached a stable configuration.

The computational domain spans from $0.88 r_H$ to $10^5 r_g$ in the radial direction, from 0 to π in the polar direction, and from 0 to 2π in the azimuthal direction, where $r_H = r_g(1 + \sqrt{1 - a^2})$ represents BH event horizon. The outer radial boundary is extended to $10^5 r_g$ using a superexponential radial grid (Ressler et al. 2017). We employ outflowing boundary conditions at the inner and outer radial boundaries, periodic in azimuth direction, and reflecting at the polar axes. While a reflective polar boundary can introduce additional dissipation near the axis (Liska et al. 2018), the overall dynamics and alignment of the prograde disks in our simulations are consistent with previous studies that used transmissive BCs (McKinney et al. 2013; Chatterjee et al. 2025).

We evolve the simulations until the inner disk ($r \leq 20 r_g$) reaches a quasi-steady state with no significant changes in its average tilt. Table 1 lists the final simulation time for each run. Following Penna et al. (2010), we define the shell-averaged quantities with density weight as:

$$\langle x \rangle_\rho(r, t) = \frac{\int_\theta \int_\phi x \rho dS_r}{\int_\theta \int_\phi \rho dS_r}, \quad (6)$$

where $dS_r = \sqrt{-g} d\theta d\phi$ is the area element of the $r =$ constant surface. In addition, for our torque analysis,

we define the area integral as:

$$[x]_{S_r}(r, t) = \int_\theta \int_\phi x dS_r \quad (7)$$

3. ALIGNMENT AND MISALIGNMENT OF PROGRADE AND RETROGRADE MADs

3.1. Accretion flow

The magnetic flux saturation at the horizon is often expressed in terms of a dimensionless quantity, ϕ_{BH} , known as the ‘‘MAD parameter’’. This parameter is defined as the ratio of the spherical magnetic flux ($\Phi_{\text{sph,BH}}$) threading the BH to the square root of the mass accretion rate (\dot{M}) at the horizon. The top panel in left column of Figure 2 shows the time evolution of the MAD parameter for $a = 0.5$ runs, where we define the spherical magnetic flux and rest-mass accretion rate as:

$$\Phi_{\text{sph}} = \frac{1}{2} \int_{\theta=0}^{\theta=\pi} \int_{\phi=0}^{\phi=2\pi} \sqrt{4\pi} |B^r| dS_r, \quad (8)$$

$$\dot{M} = - \int_{\theta=0}^{\theta=\pi} \int_{\phi=0}^{\phi=2\pi} \rho u^r dS_r \quad (9)$$

We find that $\phi_{\text{BH}} \equiv \Phi_H / \sqrt{\langle \dot{M}_{\text{BH}} \rangle_\tau r_g^2 c}$; $\Phi_H = \Phi_{\text{sph}}|_{r=r_H}$ saturates to a constant value across all the

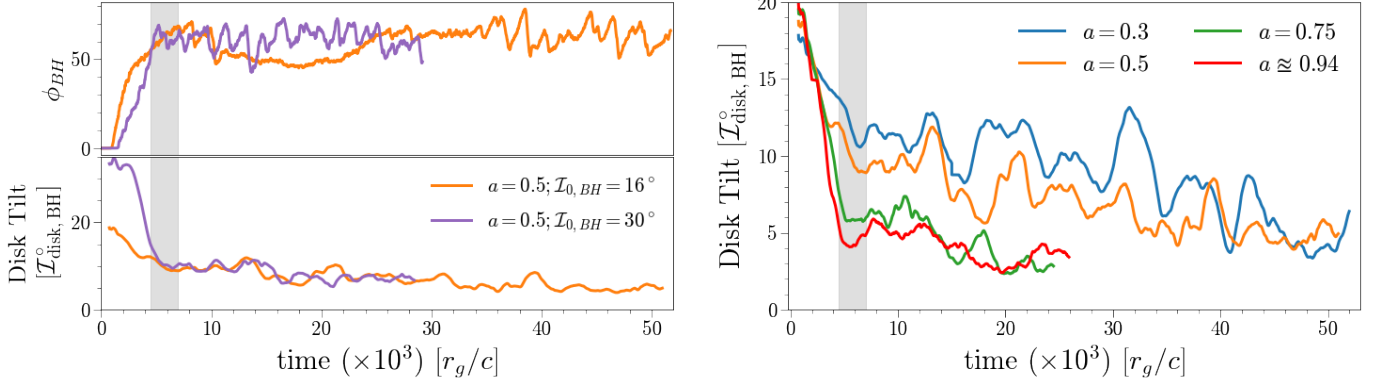


Figure 2. Left column: Top and bottom panels show the MAD parameter and the moving averages of disk tilt evolution over a timescale of $1500 r_g/c$, from the event horizon to $20 r_g$, for simulated $a = 0.5$ prograde cases (colors). **Right column:** Temporal evolution of disk tilt at different BH spins for prograde flows, each initially tilted with 16° (color-coded). The figure demonstrates that disk alignment with the BH spin occurs in two distinct stages: a rapid phase followed by a slower alignment phase. The transition, highlighted in gray, aligns with the flux saturation timescale (see Table 1).

prograde simulations (see Figure 1 for the high spin case, and Table 1 for saturated values), indicating that the magnetic flux reaches a steady equilibrium state. Here, $\langle \dot{M}_{BH} \rangle_\tau$ denotes the accretion rate at horizon, which is smoothed using a Gaussian function with a width of $\tau = 1500 r_g/c$ to highlight long-term trends.

The bottom panel in left column of Figure 2 display the time evolution of the tilt of the inner disk, measured from the horizon to $20 r_g$, for $a = 0.5$ prograde runs. We compute the disk tilt from the BH spin axis as:

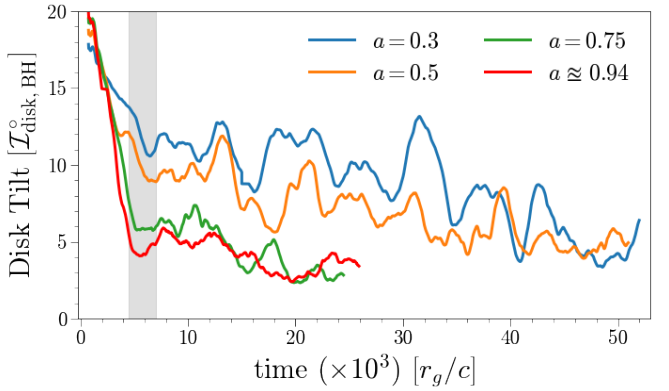
$$\mathcal{I}_{\text{disk},\text{BH}}(r,t) \equiv \cos^{-1} \left(\frac{\mathbf{L}_{BH} \cdot \langle \mathbf{L}_{\text{gas}} \rangle_\rho}{|\mathbf{L}_{BH}| |\langle \mathbf{L}_{\text{gas}} \rangle_\rho|} \right) \quad (10)$$

where \mathbf{L}_{gas} represents the disk's angular momentum and $\mathbf{L}_{BH} = a\hat{z}$ denotes the BH spin in natural units. The calculation of \mathbf{L}_{gas} ¹ follows the method outlined in Gupta & Dexter (2024):

$$(\mathbf{L}_{\text{gas}})_{\hat{k}} = \epsilon_{ijk} r^j (T^t)_{\hat{k}} \text{MA} \quad (11)$$

where the subscript “MA” signifies the matter contribution to the stress-energy tensor (Gammie et al. 2003), ϵ_{ijk} is the three-dimensional Levi-Civita symbol, and hats indicate Cartesian coordinates mapped to spherical coordinates in the conventional manner.

The bottom left panel of Figure 2 reveal several key insights. First, the tilt of the inner disk decreases steadily over time, approaching zero with the spin axis. This alignment trend persists across all prograde simulations,



regardless of initial tilt angle or spin, as shown in the right panel of Figure 2. Next, comparing the solid purple and red curves for same spin ($a = 0.5$), we observe that the initial alignment rate is higher for the 30° case than for the 16° tilt, despite both cases reaching similar MAD parameter. This implies that the alignment torque initially scales with the tilt angle. However, once a residual tilt of $\approx 8^\circ$ is reached, both systems align at nearly identical rates, suggesting a common late-stage alignment mechanism independent of initial tilt.

The temporal evolution of the disk tilt reveals two distinct alignment phases: a rapid alignment phase preceding magnetic flux saturation and a subsequent slow alignment phase, as evident in the right panel of Figure 2. The transition between these phases coincides with flux saturation, as inferred by comparing the tilt evolution (bottom) to flux growth (top). During the rapid phase, stronger spins drive a steeper decline in tilt, highlighting a strong spin dependence. This dependence diminishes in the slow phase, where alignment rate decreases significantly and converge across spins (e.g., $a = 0.3$ vs $a = 0.5$). We provide a plausible explanation for this dichotomy in Section 4.3. The highest spin case ($a \approx 0.94$) achieves nearly complete alignment, with the residual tilt of $\approx 3^\circ$ likely due to numerical errors (Gupta & Dexter 2024).

In contrast, retrograde flows never fully align, even after magnetic flux saturation. This is illustrated in Figure 1 for high-spin retrograde where we show the time evolution of the MAD parameter (middle panel) and disk tilt (bottom panel) relative to $+z$ axis. The disk tilt relative to the spin axis for retrograde runs is given by $\mathcal{I}_{\text{disk},\text{BH}}^\circ = 180^\circ - \mathcal{I}_{\text{disk},+z}^\circ$. Although high-spin retrograde does not align, its tilt relative to spin axis sometimes briefly drops by 15-20%, lasting only for

¹ We adopt extrinsic spin formulation (gauge-dependent with reference point at the BH center; Mewes et al. (2016)), rather than the intrinsic formulation (Fragile et al. 2007; McKinney et al. 2013); while all definitions yield consistent tilt/twist in the disk body, near the horizon strong curvature render the angular momentum decomposition coordinate-dependent.

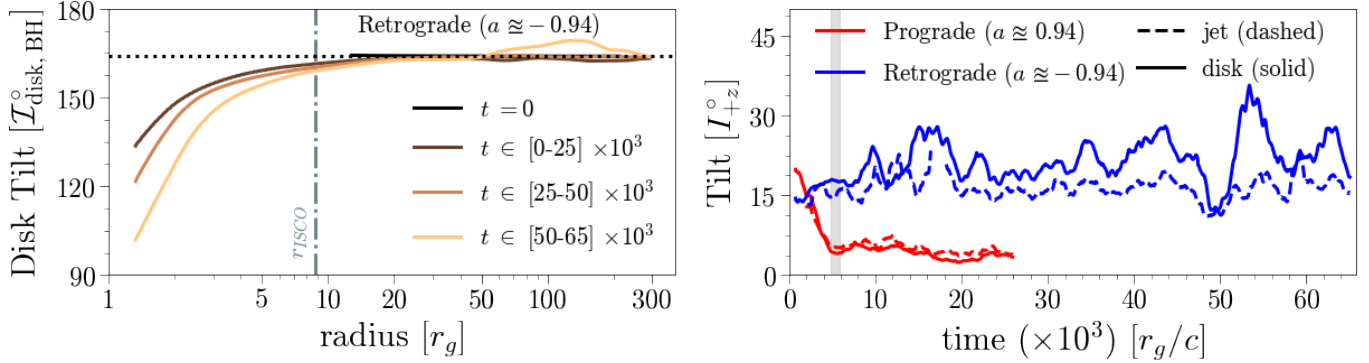


Figure 3. Left column: Density-weighted, shell-averaged radial profiles of disk tilt for the high-spin retrograde flow ($a \approx -0.94$, $I_0^o, BH = 164^\circ$), averaged over various time intervals (color-coded, in units of $10^3 r_g/c$). Within the ISCO the gas progressively shifts toward alignment with the spin axis, but never achieves complete alignment. **Right Column:** Comparing time evolution of the jet tilt (dashed) and disk tilt (solid) within the $r \in [r_H, 20 r_g]$ region for high-spin prograde (red) and retrograde (blue) flows. The prograde jets emit perpendicular to the disk midplane, aligning at a similar rate as the disk. In contrast, high-spin retrograde jet are positioned between the disk and the BH rotation axis.

$\sim 2500 r_g/c$ before swinging back toward the initial misalignment of 164° . The radial tilt profile in the left column of Figure 3 shows that inside the ISCO the disk persistently approaches orthogonality, while at larger radii it maintains its original misalignment. We observed that all of our simulated retrograde flows remained misaligned (see Table 1). Even the low-resolution $a = -0.1$ case—despite sustaining $\sim 2.5 \times$ more magnetic flux—fails to achieve lasting alignment. This indicates that alignment depends not solely on MAD parameter but also on an intricate interplay between BH spin and magnetic field strength.

3.2. Direction of the Relativistic Jet

We measured the tilt of the relativistic jet using the method proposed by Liska et al. (2018) (with a modification detailed in Appendix B) and compare them to disk tilts in the right panel of Figure 3 for high-spin prograde and retrograde case. Both quantities are tracked from the horizon to $20 r_g$. In prograde flows, the jet and disk align synchronously with minimal lag, indicating jet emission along the disk's angular momentum axis. In contrast, relativistic jets in the retrograde flow remain misaligned relative to the spin axis, mirroring the disk's orientation.

4. TORQUE ANALYSIS

4.1. Direction of the Electromagnetic Torque: What is it pointing towards?

To investigate the dynamical evolution of tilted MADs, it is crucial to study the various processes that can torque the surrounding gas. To this end, we have derived a set of equations theta govern the total angular momentum evolution in the ideal GRMHD framework—excluding contributions from any external forces

or viscosity. By “total”, we refer to the combined angular momentum of both the gas and the electromagnetic (EM) fields. The detailed derivation of these equations is presented in Appendix A.2 and A.4, where we outline the three primary sources of angular momentum flux:

1. Hydrodynamic (matter/inertial) torque, which governs angular momentum exchange between neighboring rings via the radial flux of gas
2. EM torque, driven by large-scale magnetic stresses
3. Gravitational torque due to curved spacetime.

In this analysis, we reasonably assume that the angular momentum contribution from the magnetic fields is negligible compared to the gas. Consequently, rather than focusing solely on the angular momentum derived from the matter component of the stress-energy tensor, we analyze the evolution of the total angular momentum vector to study disk alignment. Appendix A.1 provides detailed justification for this assumption. Additionally, to further explore the magnetic field's impact on average disk inclination, we perform radial surface integration (equation 7) without applying any density weighting.

Figure 4 presents the moving averages of the rate of change of disk tilt, measured from $15 r_g$ to $25 r_g$ in disk-aligned frame (see A.4), along with the contributions of different torques over a time scale of $1500 r_g/c$. The high-spin prograde ($a \approx 0.94$, tilt = 16° , left panel) and retrograde ($a \approx -0.94$, tilt = 164° , right panel) cases are shown for comparison. We selected $r \in [15, 25] r_g$ radial shell, rather than a region closer to the horizon, to avoid large numerical fluctuations and to be coherent with the rest of paper. However, we do find the following observations to be consistent for $r \geq 5 r_g$.

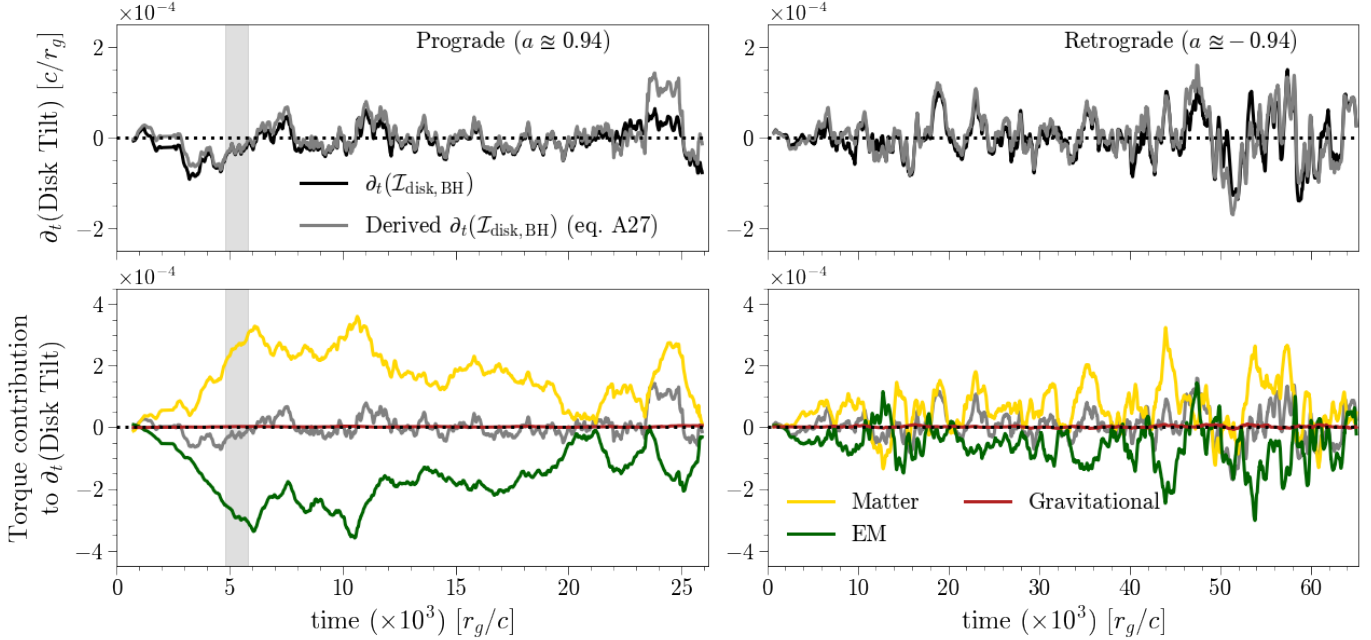


Figure 4. Torque analysis in disk-aligned frame for high-spin prograde (left column) and retrograde (right column) flows, each initially tilted by 16° relative to the $+z$ -axis. **Top:** Comparing rate of change of disk tilt (black) within $r \in [15, 25] r_g$ against our derived angular momentum evolution equations (gray; Appendix A.4) in disk-aligned frame. **Bottom:** torque contributions—gravitational (red) is negligible, EM (green) is negative for both prograde and retrograde flows, driving alignment with the spin axis. The matter torque (yellow) is always found opposing the magnetic forces, sustaining misalignment in retrograde flows.

The top panels of Figure 4 assess the accuracy of the angular momentum equations in post-processing. There is a small discrepancy between the calculated rate from the radial tilt profile and that predicted by the torque equations. It is because we did not compute the rates on the fly. The bottom panels of Figure 4 display the individual contributions of different torques—matter, EM, and gravitational. Several key observations arise from these plots. First, we observe that the contribution from gravitational torque is negligible relative to both the matter and EM torques, as expected from Lense-Thirring (LT; Lense & Thirring (1918)) torque being perpendicular to disk angular momentum vector.

More critically, we find that the EM torque contribution is negative in both the prograde and retrograde cases, and it is approximately twice as strong in the former as in the latter. This indicates that the EM fields torque the disk to align with the spin axis. In the retrograde case, this is particularly significant because the disk’s rotational axis could, in principle, become either parallel or anti-parallel. The matter torque, set by the disk’s inertia, is observed to always oppose the EM contribution and appears to adjust its magnitude in response to EM torque. In prograde disk, this opposition slows but does not prevent alignment. In retrograde flows, however, the inertial response nearly

cancels the EM torque, maintaining a quasi-steady misalignment despite the negative EM signature.

4.2. What Physical Processes Produce EM Torque and drive alignment?

To identify which electromagnetic stresses drive alignment, we decompose the x' -projected EM torque per shell. A caveat is that the tilt rate also contains a geometric shear correction (a Coriolis-like force, see A.4) arising purely from the spatial variation of the disk-aligned basis across radius, i.e. from the geometry of the annulus definition rather than a distinct channel of angular momentum flux. In practice, the shear term becomes numerically large only near the disk’s polar axes ($\theta' \rightarrow 0, \pi$). We therefore exclude the polar caps $\theta' \leq 10^\circ$ and $\theta' \geq 170^\circ$, under which we find $S_{x'} \ll \partial_r(G_{x'})$ for $r \geq 10$ and hence $\partial_t(\mathcal{I}_{+z}) \approx \frac{\partial_r G_{x'}^{\text{total}}}{|\mathbf{L}|_{S_r}|}$.

Breaking up the EM contribution of this alignment torque at a fixed radius yields:

$$\begin{aligned} \partial_r(G_{x'}^{\text{EM}}) &\equiv \partial_r [\sin \phi' T_{\theta', \text{EM}}^r + \cot \theta' \cos \phi' T_{\phi', \text{EM}}^r]_{S'_r} \\ &= \partial_r [\sin \phi' b^2 u^r u_{\theta'}]_{S'_r} - \partial_r [\sin \phi' b^r b_{\theta'}]_{S'_r} + \quad (12) \\ &\quad \partial_r [\cot \theta' \cos \phi' b^2 u^r u_{\phi'}]_{S'_r} - \partial_r [\cot \theta' \cos \phi' b^r b_{\phi'}]_{S'_r} \end{aligned}$$

where we used the fact that $r' = r$. We will refer to the first and third terms as advective EM-inertia chan-

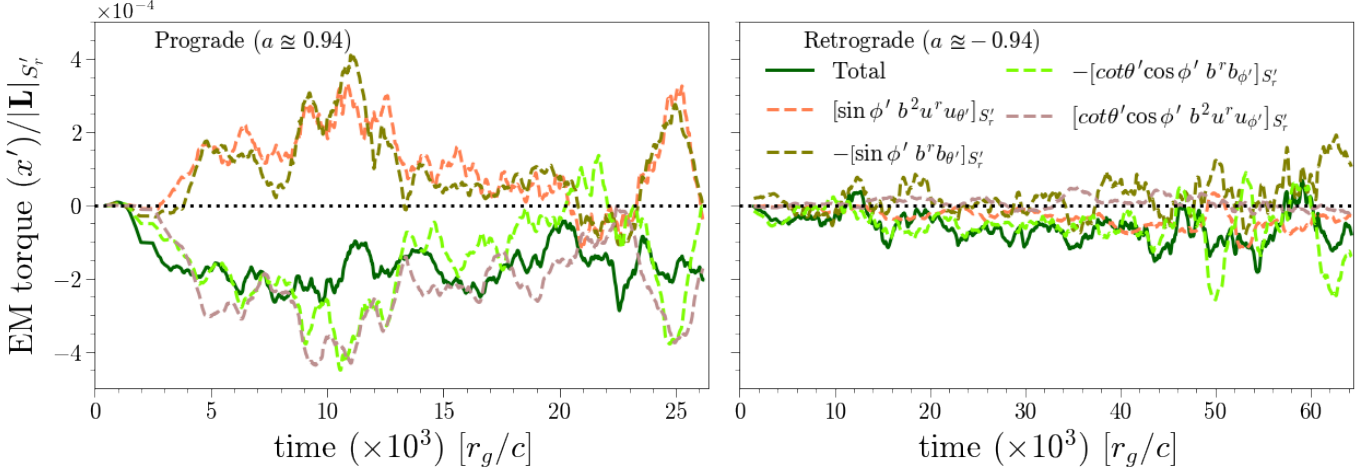


Figure 5. Electromagnetic contribution to the x' -component of $\partial_r G_{x'}^{\text{EM}} / |[\mathbf{L}]|_{S'_r}$, for high-spin prograde (left) and retrograde (right) MADs. All terms are evaluated in the disk-aligned frame for region $15 \leq r/r_g \leq 25$ with polar caps within 10° of disk polar axes are excluded. The solid dark green curve shows the net EM contribution to alignment torque. The dashed curves represent decomposition of net EM alignment torque into individual components as expressed in equation 12. Prograde runs show a net negative torque dominated by radial-azimuthal magnetic channels, whereas all magnetic channels are substantially weaker in retrograde case.

nels and to the second and fourth as Maxwell-tension channels relative to the disk orientation.

The left and right panels of Figure 5 show these contributions, normalized by $|[\mathbf{L}]|_{S'_r}$, for high-spin prograde (left) and retrograde (right) MADs in $15 r_g \leq r \leq 25 r_g$ (polar caps $\theta' \leq 10^\circ$ and $\theta' \geq 170^\circ$ excluded). The thick green curve, (sum of all EM terms; equation 12) is negative in both cases, i.e. the net magnetic forces contributes to alignment. In prograde systems, alignment is driven by large-scale radial-azimuthal magnetic tension, along with comparable $r\phi'$ EM-inertia (advective) term. By contrast, the radial-polar magnetic forces *relative to the disk orientation* enter with the opposite sign and partially offset alignment. In retrograde flows all components are weaker, intermittent alignment episodes are driven mainly by the radial-azimuthal correlation term, while the other channels fluctuate about zero with small amplitude. This contrast highlights that alignment dynamics depend sensitively on the relative orientation of the flow, while the detailed mechanisms setting the signs of individual forces remain uncertain.

4.3. An empirical model for the alignment torque: evidence for two-stage prograde disk evolution

Prograde disks and jets align in two phases (Figures 2, 3): rapid alignment operating on the flux saturation timescale, followed by a gradual residual tilt reduction. One might expect the alignment rate to peak when the flux saturates, as this marks the disk's transition to a magnetically arrested state, but we instead observe a

decline. This counterintuitive behavior may be due to weakening EM torque as the disk partially aligns.

To test this hypothesis, we investigate the patterns in alignment torque ($G_{x'}$) and shear term ($S_{x'}$) across our high-resolution runs, and ask whether their variability can be factorized into global properties of disk, such as accretion rate, tilt, magnetic pressure and/or flux. Although, there is no particular reason for a simple scaling, for small tilts considered here, the projected stress components may, to first order, scale with magnetic pressure/flux. This motivates an empirical model for alignment torque. In the top row of Figure 6, we plot time series of $G_{x'}/\Phi_H^2$ (black curve) together with instantaneous tilt (pink curve) on a twin axis for high-spin prograde and retrograde flows in $r \in [5, 25] r_g$. For prograde flows, we use $\sin \mathcal{I}_{+z}$, and for retrograde we use $-\sin \mathcal{I}_{+z}$ so that the expected handedness is the same and positive correlation implies a common driver. In both spins, the curves closely track each other; the annotated correlations are Pearson coefficients, indicating that $G_{x'} \propto \Phi_H^2 \sin \mathcal{I}_{+z}$. We find this scaling to hold well for $r < 30 r_g$.

To isolate the radial envelope, we time-averaged the ratio $\langle G_{x'} \rangle / \langle \Phi_H^2 \sin \mathcal{I}_{+z} \rangle_t$ over several time-windows and found a simple power law $f(r) \sim Ar^p$ fits all windows with minimal drift in A and p . This suggest a factorized description of alignment torque, i.e. $G_{x'} \sim f(r)\Phi_H^2 \sin \mathcal{I}_{+z}$. Furthermore, performing the same fitting for other high-res runs revealed that $A \sim k_1 \Omega_H$, where Ω_H is angular frequency of the event horizon. The fitted parameters: $k_1 \approx 2.7 \times 10^{-2}$ and p lies in

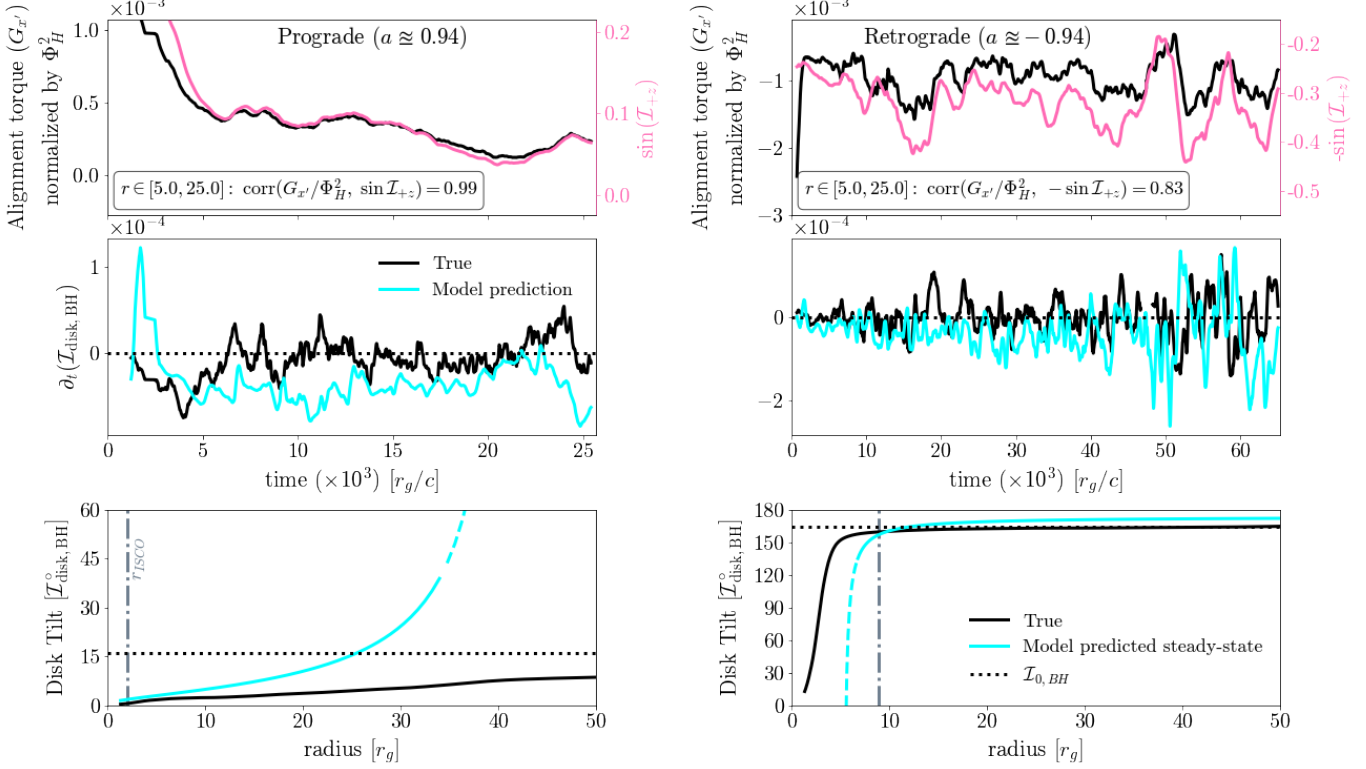


Figure 6. **Top row:** Time series of the normalized alignment torque, $G_{x'}/\Phi_H^2$ (black, left y -axis), radially integrated over $r \in [5, 25] r_g$, shown with $\sin I_{+z}$ (pink, right y -axis) for the high-spin prograde run (left column) and $-\sin I_{+z}$ for the high-spin retrograde run (right column). Annotated numbers are Pearson correlation, suggesting $G_{x'} \propto \Phi_H^2 \sin I_{+z}$ under a common sign convention. **Middle row:** Measured disk-tilt rate (black) compared to the empirical model (cyan; equation 13); the model reproduces the correct sign in the prograde run and captures episodic behavior in the retrograde run, but overpredicts the net alignment rate in both cases. **Bottom row:** Comparison of the late-time radial tilt profile, $I_{\text{disk,BH}}(r)$ (black; averaged over the final $10^4 r_g/c$), with the model steady-state prediction (cyan; equation 14). The model captures the radial trend well, but diverges as the solution approaches its singularity

the range -0.25 to -0.3 for prograde runs, and -0.55 for the high-spin retrograde case. The 30° inclined case for $a = 0.5$ shows much steeper scaling with $p \sim -0.38$. Taken together, these trends produced a simple model of alignment torque: $G_{x'} \sim k_1 r^p (\Omega_H \Phi_H^2) \sin I_{+z}$.

Next, we parametrize the shear term $S_{x'}$ (equation A29). We find that $S_{x'}(r, t) \approx -\frac{\partial I_{+z}}{\partial r} G_{z'}$ exceptionally well for prograde flows as disk aligns rapidly leaving accretion torque term the dominant force. Whereas, for retrograde, $-\partial_r(I_{+z})G_{z'}$ is still dominant (on average, 75% of shear-term comes from it), but in early times, the precession term becomes comparable as the precession profile sets early on in the disk evolution. So, keeping shear-term to first-order, we approximated $S_{x'}(r, t) \sim -\frac{\partial I_{+z}}{\partial r} G_{z'}$ for both cases, where $G_{z'} = [-T_{\phi'}^r]_{S'_r} \equiv -\dot{J}(r, t)$. Analyzing \dot{J} uncovered that $\dot{J} \sim k_2 \Omega_H \Phi_H^2(t)$ with $k_2 \approx 1.1 \times 10^{-2}$ and only weak radial variation within $r < 30 r_g$. This scaling resembles the Blandford-Znajek mechanism (Blandford & Znajek 1977; Tchekhovskoy et al. 2010) but with lower appar-

ent efficiency because angular momentum flux includes both EM and hydrodynamic contributions.

Combining these observations led to a minimal, data-driven model for the alignment rate :

$$[\partial_t(I_{+z})]_{\text{model}} \sim \frac{\Omega_H \Phi_H^2}{|\mathbf{L}|_{S_r}} \left[\frac{\partial (k_1 r^p \sin I_{+z})}{\partial r} - k_2 \frac{\partial I_{+z}}{\partial r} \right] \quad (13)$$

We confront our empirical model to the simulation data in the middle panel of Figure 6 for radial region $r \in [15, 25] r_g$. The model combines the fitted $f(r)$ with the measured $\Phi_H^2(t)$ and the disk tilt relative to the spin axis for both alignment torque and a shear-coupling correction. Without additional tuning in time, the model reproduces the correct sign of the disk tilt rate for the high-spin prograde case, and the muted, intermittent behavior in the high-spin retrograde case. However, for both cases it overestimates the alignment rate, indicating that it would not reproduce the disk tilt evolution.

Finally, setting $[\partial_t(I_{+z})]_{\text{model}} = 0$ gives the following differential equation, which under small-tilt approxima-

tion yields:

$$k_1 \frac{d(r^p \sin \mathcal{I}_{+z})}{dr} = k_2 \frac{d\mathcal{I}_{+z}}{dr}$$

$$\mathcal{I}_{+z}(r) \sim \frac{C}{k_1 r^p - k_2} \quad (14)$$

where the final step uses small-tilt approximation and C is an integration constant. For our fitted parameters: $k_1 \approx 2.7 \times 10^{-2}$ and $k_2 \approx 1.1 \times 10^{-2}$, the above solution has a singular point at $r_s = (k_2/k_1)^{1/p} > 0$, where the solution changes behavior. For instance, if $(k_1 r^p - k_2) > 0$ and $r < r_s$, the disk tilt (relative to $+z$ axis) increases with radius, and decreases for $r > r_s$. Whereas, for $(k_1 r^p - k_2) < 0$ the trend changes. Furthermore, the singular point moves outward as p becomes less negative. For instance, for $a = 0.75$ and 0.9375 with $p \sim -0.32$ and -0.24 , we find $r_s \sim 16 r_g$ and $42 r_g$, whereas for retrograde, we noted $r_s \sim 5 r_g$.

We compare the steady-state profiles of disk tilt for our high-spin prograde and retrograde cases against the steady-state profile predicted by the model in the bottom row of Figure 6. We calculated $C = (k_1 r_{ref}^p - k_2) \mathcal{I}_{+z}|_{r_{ref}}$, where we fixed $r_{ref} = 10 r_g$ as the system reached the viscous equilibrium there and our derived torques are valid only for $r \geq 5 r_g$. The plot shows that the model captures the correct radial trend in both cases, especially for the retrograde run. The cause for it lies in the fact that $k_1 r^p - k_2 < 0$ for $r > r_s$ in retrograde case, producing decreasing \mathcal{I}_{+z} with radius, and hence increasing radial profile of disk tilt relative to the spin axis. Close to the singular radius, the model prediction diverges as expected.

Even though model has its limitations, we can still address the question of two-stage prograde alignment. In the pre-MAD era during which *radial profile of tilt is nearly constant*, the alignment rate for a fixed spin is: $\partial_t(\mathcal{I}_{BH})_{\text{rapid}} \propto p k_1 \Phi_H^2 \sin \mathcal{I}_{BH} r^{p-1}$, i.e. relatively stronger as the magnetic flux advects onto the hole. However, after the disk becomes MAD, $\Phi_H^2 \sin \mathcal{I}_{BH}$ decreases substantially leading to reduction in alignment rate. Furthermore the faster alignment at smaller radius produces $\partial_r(\mathcal{I}_{disk, BH}) > 0$, leaving $\partial_r(G_{x'}) > 0$ in post-MAD era. The slow yet non-zero alignment rate comes from the shear-coupling term: $-k_2 \Omega_H \Phi_H^2 \partial_r(\mathcal{I}_{BH})$, which loosely quantifies the efficiency of accretion torque in reorienting the disk as it redistributes angular momentum across a warp.

5. SOLID-BODY PRECESSION OF THE RETROGRADE MADS

Building on our finding that retrograde MADs do not align, we measured the precession of the disk about the

fixed $+z$ -axis, following the definition from [Gupta & Dexter \(2024\)](#):

$$\mathcal{P}_{\text{disk}}(r, t) = \tan^{-1} \left(\frac{\langle L_{y, \text{gas}} \rangle_{\rho}}{\langle L_{x, \text{gas}} \rangle_{\rho}} \right) \quad (15)$$

The left panel of Figure 7 shows the total disk precession angle for each retrograde MAD run in the region $10 r_g \leq r \leq 100 r_g$ region. The high resolution $a \approx -0.94$ is shown as a solid, thick blue line, while the low-resolution cases appear as thin, dashed colored curves. The negative angles indicating clockwise motion in the same direction as the BH's rotation. We find that precession rate grows with increasing spin magnitude, and in the high-spin retrograde run doubling the initial tilt from 16° to 30° (relative to $+z$ -axis) increases the precession frequency by roughly 50%. Although the low-resolution run hint at a tilt dependence, their coarse resolution may also amplify the precession rate ([Liska et al. 2018](#); [Chatterjee et al. 2020](#)).

We compare our observations to the analytic model of [Fragile et al. \(2007\)](#) in the right panel of Figure 7, assuming inner and outer disk radius of $r_i \sim 10 r_g$ and $r_o \sim 100 r_g$, and surface density slope $\zeta \sim -0.5$, derived from the surface density profile $\Sigma = \Sigma_i(r/r_i)^{-\zeta}$ for the high-spin retrograde run with tilt = 164° . We find that the observed precession period is consistently 2–5 times shorter than the analytical estimate across all simulated spins, suggesting a faster precession rate than the frequency of a test-particle at the radius of the disk's mean angular momentum.

6. DISCUSSION

6.1. Can the Retrograde MADs Align?

Our results demonstrate that high-spin retrograde MADs exhibit cyclical alignment tendencies, yet gas inertia ultimately counteracts magnetic forces, preventing complete alignment (Figure 1 and 4). This raises a critical question: under what conditions, if any, can retrograde MADs achieve mutual alignment with the BH spin? To discuss it, we re-write equation A27 for *retrograde tilts* as:

$$|\mathbf{L}|_{S_r} \partial_t(\mathcal{I}_{BH}) = -\partial_r(\tau_{x'}) + \mathcal{S}_{x'} \quad (16)$$

The above equation dictates that for retrograde flows to align the net action of alignment force and the shear-term should be negative. Assuming our empirical model holds at larger tilts and horizon magnetic flux remain constant, it suggest that the alignment torque grows with misalignment and decreases with radius. Thus, $-\partial_r(\tau_{x'})$ should be more negative at larger tilts and BH spin magnitude.

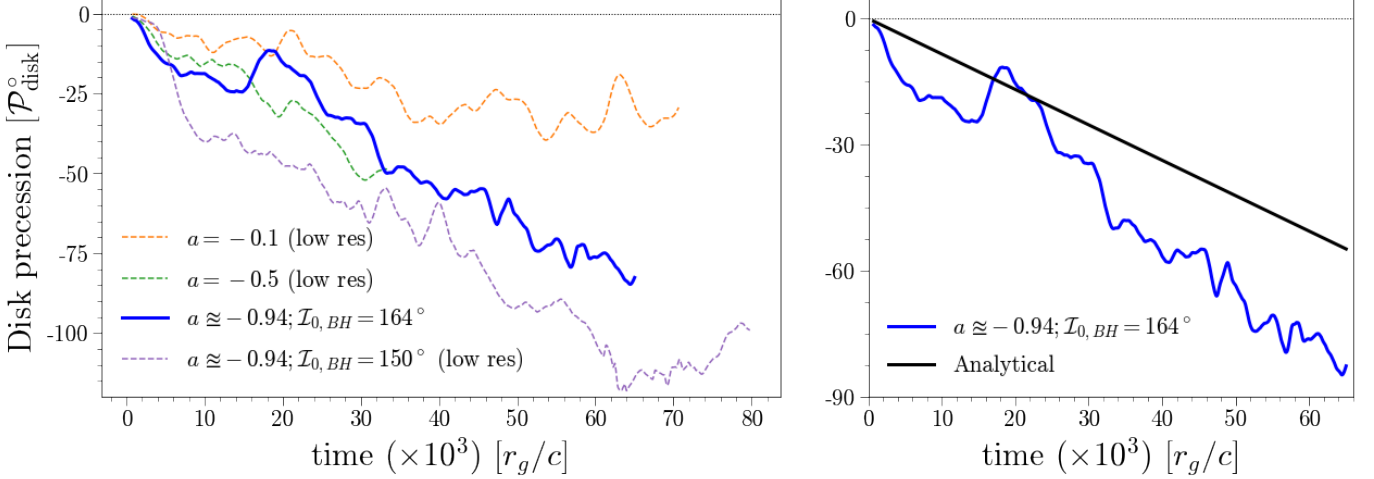


Figure 7. **Left:** Disk precession angle, $\mathcal{P}_{\text{disk}}(t)$ (equation 15) integrated over $r \in [10, 100] r_g$, for retrograde MADs with different spins and initial tilts (legend). The high-resolution $a \simeq -0.94$, $\mathcal{I}_{0, \text{BH}} = 164^\circ$ run is shown as the solid blue curve; dashed curves denote lower-resolution runs. Negative $\mathcal{P}_{\text{disk}}$ corresponds to clockwise precession, i.e., in the same sense as the BH rotation. **Right:** High-spin retrograde case ($a \simeq -0.94$, $\mathcal{I}_{0, \text{BH}} = 164^\circ$; blue) compared to the rigid-body precession prediction of Fragile et al. (2007) (black; evaluated for $r_i \simeq 10 r_g$, $r_o \simeq 100 r_g$, and $\zeta \simeq -0.5$). The simulated precession is faster, with a period $\sim 2\text{--}5 \times$ shorter than the analytic estimate.

For the shear-term, which is positive in our retrograde models and thus opposes alignment, we therefore expect the approximation $\mathcal{S}_{x'} \approx \partial_r(\mathcal{I}_{BH})G_{z'}$ (for retrograde) to remain relevant at larger tilts. First, increasing tilt reduces $\cos \mathcal{I}_{BH}$, so the second term contribution $\propto -G_{y'}^{\text{MA+EM}} \cos \mathcal{I}_{BH} \partial_r(\mathcal{P})$ in shear-term (equation A29) is naturally suppressed. Second, if radial twist profile is set by LT torque, then one may estimate $\partial_r(\mathcal{P}) \sim \Omega_{LT}/|v^r|$, with $\Omega_{LT} \propto r^{-3}$ and $v_r \sim r^{-1}$ in MAD simulations (Narayan et al. 2022), so $\partial_r(\mathcal{P}) \propto r^{-2}$ and hence, the combination $\cos \mathcal{I}_{BH} \partial_r(\mathcal{P})$ is expected to decrease with increasing tilt at fixed radius. Finally, local maxwell stress associated with accretion is expected to dominate relative to precessional torque: $G_{y'}$ which is arising because of stress projections, indicating $G_{z'} > G_{y'}$. Under these assumptions the shear term should effectively scales as $\partial_r(\mathcal{I}_{BH})G_{z'}$. Moreover, recent simulations of Chatterjee et al. (2025) indicate that jet power (and thus the associated EM torque) declines with increasing tilt, implying $G_{z'}$ is likely reduced at larger misalignment, further weakening this opposing geometric term.

Combining these trends suggests that there may exist a critical tilt angle beyond which the growth of the alignment torque with misalignment can outweigh the weakening shear term in the inner MAD region. In such a regime the retrograde flow could, in principle, drive toward a mutually aligned state. Conversely, if the alignment torque saturates or scales only a $\sin \mathcal{I}_{BH} \cos \mathcal{I}_{BH}$, its growth with misalignment would be too weak and hot retrograde MADs would remain persistently misaligned.

Distinguishing between these possibilities requires simulations that explicitly measure the tilt dependence of the alignment torque (see section 6.4).

6.2. Precession of Prograde Flows and the Jet

Relativistic jets in retrograde flows, which do not emit along the BH rotation axis, may undergo precession (Liska et al. 2018; Chatterjee et al. 2025). For the weakly rotating BH ($a = -0.1$), we observe precession of the jet occurring at a rate comparable to the disk. At higher spins, however, numerical fluctuations in the jet’s twist angle—driven by inflowing gas disrupting magnetized regions ($\sigma > 1$)—preclude robust measurement of precession period. Nevertheless, the observed $a = -0.1$ behavior and our setup’s similarity to Chatterjee et al. (2025) suggest jet precession remains plausible in astrophysical systems.

While investigating precession in prograde flows, we observed an unexpected pattern. Although near-complete alignment during flux saturation should render precession moot, tracking the twist angle over time reveals prograde precession, followed by a transition to clockwise, retrograde, solid-body precession in slow-alignment phase. The same phenomenon is also observed by Jiang et al. (2025). To validate this, we ran a low resolution, high-spin BH ($a \simeq -0.94$) with a 164° -tilted torus, effectively simulating a prograde case. Here, too, the disk precess opposite to the BH spin. Analyzing precession torque gradient $\partial_r(G_{y'})$ (as $\mathcal{S}_{y'} \ll \partial_r(G_{y'})$ in equation A28 for $r \geq 10 r_g$) revealed that inertial torques dominate as gravitational torques weaken dur-

ing rapid alignment, driving this counter-rotating precession. However, more in-depth analysis is needed to conclude it.

6.3. Comparison to Previous Works

Our results broadly agree with prior GRMHD studies of misaligned tori (McKinney et al. 2013; Chatterjee et al. 2025), confirming that prograde MADs align post flux saturation, even for spins as low as $a = 0.3$, supporting the hypothesis from McKinney et al. (2013) that magneto-spin alignment may be achievable for most or all geometrically thick, prograde MAD spins. Like McKinney et al. (2013), we find disk-jet alignment within $50 r_g$ for prograde flows, with divergence at larger radii attributed to jet interactions with inflowing gas.

A key discrepancy arises for retrograde MADs: while McKinney et al. (2013) reported disk flipping and eventual alignment of it with the spin, our retrograde flows remain misaligned. This difference likely stems from how tilt is introduced. In McKinney et al. (2013), the relative tilt between the disk (and magnetosphere) and the BH was imposed mid-simulation by rotating the spin axis in a previously aligned MAD. This preserved magnetic flux levels comparable to prograde cases, as noted in (McKinney et al. 2012, Table 9), enabling strong alignment torques. In contrast, initial tilt introduction in our setup suppresses flux saturation in retrograde flows, weakening magnetic torques below the threshold for alignment.

Our torque decomposition further suggests that the hydrodynamic flux is not merely a residual term: it can respond to the magnetic alignment torque and thereby modulate the net alignment rate (Section 4). Prior simulations show robust alignment in prograde MADs (except at very large tilts; Chatterjee et al. (2025)) but incomplete alignment and enhanced warping in more weakly magnetized SANE-like flows (Fragile et al. 2007; White et al. 2019; Gupta & Dexter 2024); this leaves open the possibility that a relatively narrow range of horizon-threading magnetic flux separates these regimes, with the transition potentially complicated by temporal flux variability (White et al. 2020).

Another difference concerns the physical interpretation of the alignment mechanism. In our simulations the jet and inner disk align on similar rate, and the jet axis remains nearly perpendicular to the disk plane, which makes it difficult for the jet alone to provide the lateral torque needed to reorient the disk. Instead, our torque decomposition indicates that the dominant contribution to $G_{x'}$ which led the initial rapid alignment arises from the in-plane $T'_{\phi'}$ stress projected into the tilted basis, i.e. from non-axisymmetric magnetic cor-

relations within the disk rather than from the axisymmetric component that primarily feeds the jet. Because these stresses may still scale with the horizon magnetic flux, the net alignment torque may superficially resembles a jet-driven picture, even if the underlying torques are disk-driven. We therefore interpret magneto-spin alignment in our models as being mediated mainly by internal disk stresses, while noting that a more quantitative separation of jet and disk contributions will require analysis over a wider range of tilts and magnetic strength.

6.4. Validity of the Empirical Model

In section 4.3, we modeled alignment torque as: $G_{x'} \propto \Phi_H^2 \sin \mathcal{I}_{+z}$. A related form $G_{x'} \propto \Phi_H^2 \sin \mathcal{I}_{+z} \cos \mathcal{I}_{+z}$ shows a comparably good correlation, except very close to the horizon in retrograde flows. Because our simulations only probe modest tilts, we cannot robustly distinguish between these functional forms, and the explicit tilt dependence of the alignment torque remains poorly constrained. An additional factor such as $\cos \mathcal{I}_{+z}$ could help explain why the extremely misaligned disks in Chatterjee et al. (2025) do not align.

A further limitation is the degeneracy in how the torque scales with magnetic strength. While we have parameterized the alignment torque in terms of Φ_H , similar if not better correlations are obtained with local magnetic flux or magnetic pressure. Since disk alignment ultimately depends on the local angular-momentum flux, it is plausible that scaling $G_{x'}$ and $G_{y'}$ with local magnetic pressure would provide a more accurate description at larger radii; we have retained Φ_H here because it displayed moderately better correlations in prograde flows. Finally, our empirical model is constructed for the net torque. It is possible that a simple flux-based scaling applies more cleanly to the EM component alone, particularly in tilted, weakly magnetized (SANE-like) flows.

7. CONCLUSION

In this study, we set out to elucidate the alignment processes in tilted MADs around BHs of varying spin parameters. Using a set of global, ideal 3D GRMHD simulations we explored accretion scenarios with spins ranging from $a = -0.1$ to $a = 0.9375$, incorporating initial disk tilts of 16° and/or 30° relative to the $+z$ -axis. The primary findings of our study are as follows:

1. Tilted prograde MADs achieve mutual alignment with the BH spin axis through a two-stage process. The disk first undergoes rapid alignment on the magnetic flux saturation timescale, followed by a slower phase in which the inner disk continues to align at a reduced but measurable rate.

2. Retrograde MADs remain persistently misaligned and exhibited near-solid body precession, with periods $\sim 10^5 r_g/c$, consistent with the ~ 0.2 Hz Type-C QPOs observed in $\sim 10 M_\odot$ black hole X-ray binaries (Ingram et al. 2016; Liska et al. 2019). In both prograde and low-spin retrograde systems, jets emerge perpendicular to the inner disk midplane.
3. EM torques are the primary drivers of disk alignment in both prograde and retrograde MADs—but with significantly greater strength in prograde flows. In retrograde cases, opposing hydrodynamic torques, effectively counterbalance the EM torque, preventing alignment, while gravitational torques remain negligible.
4. Evaluating the EM contribution to the alignment torque with narrow polar caps excluded shows that the (projected) radial–azimuthal magnetic stress is the primary driver of prograde alignment, while in

retrograde flows all EM channels are substantially weaker.

5. Across the high-resolution runs, the net alignment torque per shell is well described by a separable scaling $G_{x'} \propto f(r) \Omega_H \Phi_H^2 \sin \mathcal{I}_{+z}$ with a shallow $f(r)$, which preliminary explained the observed two-stage prograde alignment but our empirical model systematically overestimates the simulation-measured tilt rate.

¹ S.G. gratefully acknowledges stimulating discussions with M. C. Begelman, K. Long, C. Echiburú-Trujillo, P. Dhang, and J. Jacquemin Ide. This work was supported in part by NASA Astrophysics Theory Program grant 80NSSC24K1094 and Chandra awards TM3-24003X and TM4-25005X.

Software: Matplotlib (Hunter 2007), NumPy (Harris et al. 2020)

APPENDIX

A. RATE OF CHANGE OF ANGULAR MOMENTUM

The goal of this section is to provide a rationale for the use of total angular momentum to study the disk tilt and to elucidate the identification of torque components while deriving the evolution equations of the angular momentum.

A.1. *Tilt using total angular momentum*

Similar to equation 11, we define the total angular momentum density, including both gas and magnetic fields, as:

$$(\mathbf{L}_{\text{total}})_{\hat{k}} = \epsilon_{ijk} r^{\hat{j}} (T^t_{\hat{k}}), \quad (\text{A1})$$

where T^μ_ν is the total stress-energy tensor and the subscript “total” signifies the combined contribution. The total angular momentum vector serves as a reliable indicator of disk tilt for two main reasons. First, the magnetic field’s inertia is negligible relative to the gas, making $(\mathbf{L}_{\text{total}})_{\hat{k}} \approx (\mathbf{L}_{\text{gas}})_{\hat{k}}$. Second, tilt and twist are angular properties expressed through the ratio of angular momentum components (see equations 10 and 15), and thus are not influenced by the absolute magnitude of any single component. Figure 8 validates the approximation by comparing disk tilt (from section 3) to tilt derived from total angular momentum (equation A1) as:

$$\mathcal{I}_{\text{total,BH}}(r, t) \equiv \cos^{-1} \left(\frac{\mathbf{L}_{BH} \cdot [\mathbf{L}_{\text{total}}]_{S_r}}{|\mathbf{L}_{BH}| |[\mathbf{L}_{\text{total}}]_{S_r}|} \right), \quad (\text{A2})$$

where $[x]_{S_r}$ is the area integral (equation 7). We did not use density-weighting in equation A1 to ensure the contributions from highly magnetized regions as well as the high-density areas are on same footing. While the comparison in Figure 8 covers the radial range $[3, 20] r_g$, we found this approximation to hold true up to $300 r_g$, the extent of the initial torus. However, close to the horizon, magnetic contributions rival gas inertia leading to the breakdown of the approximation.

A.2. *Torque equations*

Building on the rationale for using total angular momentum density to study disk tilt, we derive the torque equations governing total angular momentum evolution. *For the following sections, we report every quantity relative to +z axis*

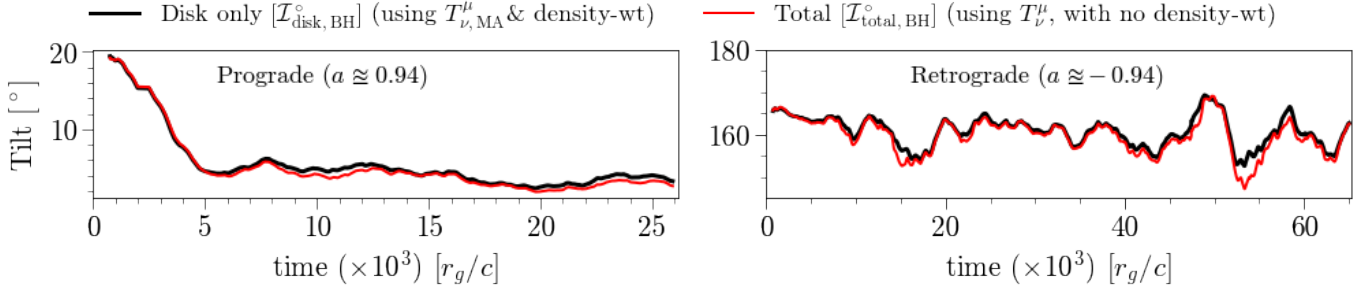


Figure 8. Time evolution of the disk tilt in the inner region $r \in [3, 20] r_g$, comparing the density-weighted tilt computed from $T^{\mu}_{\nu, \text{MA}}$ (black; equations 11 and 10) to the total tilt computed from T^{μ}_{ν} without density weighting (red; equations A1 and A2), for high-spin prograde (left) and retrograde (right) runs with initial tilt 16° relative to $+z$. This comparison motivates using the total tilt when analyzing the disk angular-momentum evolution.

of the simulation frame. We begin by expressing the total angular momentum components in Cartesian coordinates, where the stress-energy tensor components are described in spherical coordinates. The total angular momentum in a spherical region of radius ‘ r ’ at a fixed time is given by:

$$\begin{aligned} \int_{r_i}^r L_{x, \text{total}} dV &= \int_{r_i}^r (-\sin \phi T_{\theta}^t - \cot \theta \cos \phi T_{\phi}^t) dV \\ \int_{r_i}^r L_{y, \text{total}} dV &= \int_{r_i}^r (\cos \phi T_{\theta}^t - \cot \theta \sin \phi T_{\phi}^t) dV, \\ \int_{r_i}^r L_{z, \text{total}} dV &= \int_{r_i}^r T_{\phi}^t dV, \end{aligned} \quad (\text{A3})$$

where $dV = \sqrt{-g} dr d\theta d\phi$ is the proper volume element. To obtain the time evolution of the angular momentum in this control volume, we differentiate equation A3 and use energy–momentum conservation (2) to express the rate in flux form as

$$\partial_t (\sqrt{-g} T^t_{\nu}) = -\partial_i (\sqrt{-g} T^i_{\nu}) + \sqrt{-g} T^{\kappa}_{\lambda} \Gamma^{\lambda}_{\nu\kappa}, \quad (\text{A4})$$

For a stationary, axisymmetric metric we have $\partial_t \sqrt{-g} = 0$, and the azimuthal Killing symmetry implies $\sqrt{-g} T^{\kappa}_{\lambda} \Gamma^{\lambda}_{\nu\kappa} = 0$. Substituting equation A4 into the definitions of L_i and using the product rule to absorb the trigonometric prefactors into the divergence terms, we obtain

$$\begin{aligned} \partial_t \left(\int_{r_i}^r L_{x, \text{total}} dV \right) &= \int_{r_i}^r \partial_i (\sqrt{-g} \sin \phi T_{\theta}^i) dr d\theta d\phi + \int_{r_i}^r \partial_i (\sqrt{-g} \cot \theta \cos \phi T_{\phi}^i) dr d\theta d\phi + \\ &\quad - \int_{r_i}^r \sin \phi T_{\lambda}^{\kappa} \Gamma_{\theta\kappa}^{\lambda} dV + \int_{r_i}^r \left(\cot \theta \sin \phi T_{\phi}^{\phi} + \frac{\cos \phi}{\sin^2 \theta} T_{\phi}^{\theta} - \cos \phi T_{\theta}^{\phi} \right) dV \end{aligned} \quad (\text{A5})$$

$$\begin{aligned} \partial_t \left(\int_{r_i}^r L_{y, \text{total}} dV \right) &= - \int_{r_i}^r \partial_i (\sqrt{-g} \cos \phi T_{\theta}^i) dr d\theta d\phi + \int_{r_i}^r \partial_i (\sqrt{-g} \cot \theta \sin \phi T_{\phi}^i) dr d\theta d\phi + \\ &\quad + \int_{r_i}^r \cos \phi T_{\lambda}^{\kappa} \Gamma_{\theta\kappa}^{\lambda} dV + \int_{r_i}^r \left(-\cot \theta \cos \phi T_{\phi}^{\phi} + \frac{\sin \phi}{\sin^2 \theta} T_{\phi}^{\theta} - \sin \phi T_{\theta}^{\phi} \right) dV \end{aligned} \quad (\text{A6})$$

$$\partial_t \left(\int_{r_i}^r L_{z, \text{total}} dV \right) = \int_{r_i}^r [\partial_i (-\sqrt{-g} T_{\phi}^i)] dr d\theta d\phi \quad (\text{A7})$$

We now focus on each component individually, beginning with the axisymmetric ‘ z ’ component. The RHS of equation A7 represents the net flux of azimuthal momentum out of the control volume at a given time. Since we study the local rate of change of total angular momentum in the Eulerian frame and in the 3+1 decomposition of spacetime, the control volume, fixed in space, corresponds to a hypersurface of constant time. This allows us to rewrite the RHS

in terms of proper volume integration. Applying the Gauss-divergence theorem (Misner et al. 1973; E. 2000; Carroll 2003), we obtain:

$$\partial_t \left(\int_{r_i}^r L_{z,\text{total}} dV \right) = \int_{r_i}^r [\partial_i (-\sqrt{-g} T_\phi^i)] dr d\theta d\phi = - \int_{r_i}^r \nabla_i (\sqrt{-g} T_\phi^i) dV = \left(- \int T_\phi^r dS_r \right) \Big|_{r_i}^r \quad (\text{A8})$$

Performing the same set of operations for equations A5 and A6 gives:

$$\begin{aligned} \partial_t \left(\int_{r_i}^r L_{x,\text{total}} dV \right) &= \left(\int (\sin \phi T_\theta^r + \cot \theta \cos \phi T_\phi^r) dS_r \right) \Big|_{r_i}^r - \int_{r_i}^r \sin \phi T_\lambda^\kappa \Gamma_{\theta\kappa}^\lambda dV + \\ &\quad \int_{r_i}^r \left(\cot \theta \sin \phi T_\phi^\phi + \frac{\cos \phi}{\sin^2 \theta} T_\phi^\theta - \cos \phi T_\theta^\phi \right) dV \end{aligned} \quad (\text{A9})$$

$$\begin{aligned} \partial_t \left(\int_{r_i}^r L_{y,\text{total}} dV \right) &= \left(\int (-\cos \phi T_\theta^r + \cot \theta \sin \phi T_\phi^r) dS_r \right) \Big|_{r_i}^r + \int_{r_i}^r \cos \phi T_\lambda^\kappa \Gamma_{\theta\kappa}^\lambda dV + \\ &\quad \int_{r_i}^r \left(-\cot \theta \cos \phi T_\phi^\phi + \frac{\sin \phi}{\sin^2 \theta} T_\phi^\theta - \sin \phi T_\theta^\phi \right) dV \end{aligned} \quad (\text{A10})$$

The equations above give the time rate of change of the total angular-momentum components enclosed within a closed spherical-shell volume between r_i and r . To study the radial structure and time-averaged profiles of disk tilt and twist, we require the corresponding *local* evolution at each radius. Following Sorathia et al. (2013), we take a radial derivative and apply the Leibniz rule to convert the volume integrals into surface terms evaluated at r . We then decompose T^μ_ν into matter and electromagnetic parts (Gammie et al. 2003) to isolate the contributions from different torque channels, yielding the expressions below.

$$\partial_t \left(\int L_{z,\text{total}} dS_r \right) = \partial_r (G_z) \equiv \underbrace{-\partial_r \left(\int (L_{z,\text{gas}} V^r) dS_r \right)}_{\text{Matter torque (z-comp)}} - \underbrace{\partial_r \left(\int T_{\phi,\text{EM}}^r dS_r \right)}_{\text{EM torque (z-comp)}}, \quad (\text{A11})$$

$$\begin{aligned} \partial_t \left(\int L_{x,\text{total}} dS_r \right) = \partial_r (G_x) \equiv & \underbrace{-\partial_r \left(\int (L_{x,\text{gas}} V^r) dS_r \right)}_{\text{Matter torque (x-comp)}} + \underbrace{\partial_r \left(\int (\sin \phi T_{\theta,\text{EM}}^r + \cot \theta \cos \phi T_{\phi,\text{EM}}^r) dS_r \right)}_{\text{EM torque (x-comp)}} + \\ & \underbrace{\int \left(-\sin \phi T_\lambda^\kappa \Gamma_{\theta\kappa}^\lambda + \cot \theta \sin \phi T_\phi^\phi + \frac{\cos \phi}{\sin^2 \theta} T_\phi^\theta - \cos \phi T_\theta^\phi \right) dS_r}_{\text{Gravitational torque (x-comp)}}, \end{aligned} \quad (\text{A12})$$

$$\begin{aligned} \partial_t \left(\int L_{y,\text{total}} dS_r \right) = \partial_r (G_y) \equiv & \underbrace{-\partial_r \left(\int (L_{y,\text{gas}} V^r) dS_r \right)}_{\text{Matter torque (y-comp)}} + \underbrace{\partial_r \left(\int (-\cos \phi T_{\theta,\text{EM}}^r + \cot \theta \sin \phi T_{\phi,\text{EM}}^r) dS_r \right)}_{\text{EM torque (y-comp)}} + \\ & \underbrace{\int \left(\cos \phi T_\lambda^\kappa \Gamma_{\theta\kappa}^\lambda - \cot \theta \cos \phi T_\phi^\phi + \frac{\sin \phi}{\sin^2 \theta} T_\phi^\theta - \sin \phi T_\theta^\phi \right) dS_r}_{\text{Gravitational torque (y-comp)}}, \end{aligned} \quad (\text{A13})$$

where $V^r \equiv u^r/u^t$ is the radial coordinate three-velocity, and $L_{i,\text{gas}}$ is the gas-only angular-momentum density (equation 11), i.e., the matter contribution to the volume integral in equation A3. The quantities G_i denote the components

of the total torque vector (gas plus fields) in the simulation frame. This decomposition shows that the matter torque is set by the radial flux of gas angular momentum, while the electromagnetic torque arises from the divergence of the Maxwell stress, consistent with [Sorathia et al. \(2013\)](#). We define the total angular momentum magnitude as as $|\mathbf{L}_{\text{total}}|_{S_r} \equiv \sqrt{[L_{x,\text{total}}]_{S_r}^2 + [L_{y,\text{total}}]_{S_r}^2 + [L_{z,\text{total}}]_{S_r}^2}$. The next section describes our procedure for isolating the gravitational torque.

A.3. Identification of Gravitational torque

We identify the terms involving the metric connection ($T^\kappa_\lambda \Gamma^\lambda_{\theta\kappa}$) and the mixed $\theta\phi$ and $\phi\phi$ stresses in equations [A12–A13](#) as the gravitational-torque contribution. Below we validate this identification by showing that it reduces to the expected Lense-Thirring (LT) torque ([Lense & Thirring 1918](#)) in the weak-field limit.

We first examine the connection term $T^\kappa_\lambda \Gamma^\lambda_{\theta\kappa}$, which encodes latitudinal forces produced by curved spacetime, centrifugal and magnetic hoop stress, as well as other complex interactions that are not straightforward to interpret ([Scepi et al. 2023](#)). While $\Gamma^\lambda_{\theta\kappa}$ can be written in terms of metric gradients, its contraction with T^κ_λ makes the dominant contribution non-obvious. Guided by several simulations (this work, [Gupta & Dexter 2024](#), and the aligned high-spin MAD of [Dexter et al. 2020](#)), we find that for $r \gg a$ the contraction is well-approximated by two toroidal-stress terms:

$$T^\kappa_\lambda \Gamma^\lambda_{\theta\kappa} \approx T_\phi^\phi \Gamma_{\theta\phi}^\phi + T_\phi^t \Gamma_{\theta t}^\phi \quad (\text{A14})$$

This behavior is consistent with the predominantly azimuthal motion of a weakly tilted flow and the buildup of toroidal magnetic stress, though we do not attempt a first-principles derivation. We next test whether our “gravitational” terms reproduce the LT form in the weak-field regime, i.e. $\boldsymbol{\Omega}_{\text{LT}} \times \mathbf{L}_{\text{total}} = \{-\Omega_{LT} L_{y,\text{total}}, \Omega_{LT} L_{x,\text{total}}, 0\}$ with $|\boldsymbol{\Omega}_{\text{LT}}| = 2a/r^3$ aligned with the BH spin axis

To approximating T_ϕ^θ and $T_\lambda^\kappa \Gamma^\lambda_{\theta\kappa}$, we write the line element in the weak-field approximation ($a \ll 1$) ([Lense & Thirring 1918; Adler et al. 1965](#)):

$$ds^2 = - \left(1 - \frac{2}{r}\right) dt^2 + \left(1 + \frac{2}{r}\right) dr^2 + r^2 (d\theta^2 + \sin^2 \theta d\phi^2) - \frac{4a \sin^2 \theta}{r} d\phi dt, \quad (\text{A15})$$

and use tensor transformation rules to re-write equation [A14](#) as:

$$T_\phi^\theta \approx -\frac{2a \sin^2 \theta}{r^3} T_\theta^t + \sin^2 \theta T_\theta^\phi; \quad T_\lambda^\kappa \Gamma^\lambda_{\theta\kappa} \approx T_\phi^\phi \Gamma_{\theta\phi}^\phi + T_\phi^t \Gamma_{\theta t}^\phi \approx \cot \theta T_\phi^\phi - \frac{2a \cot \theta}{r^3} T_\phi^t, \quad (\text{A16})$$

valid for $a \ll 1$ and $r \gg a$. Substituting above equation into gravitational torque expressions (equation [A12](#) and [A13](#)) yields:

$$\partial_r (G_x^{\text{gravity}}) \approx \int \frac{2a}{r^3} (-\cos \phi T_\theta^t + \cot \theta \sin \phi T_\phi^t) dS_r \approx \int_\theta \int_\phi (-|\boldsymbol{\Omega}_{\text{LT}}| L_{y,\text{total}}) dS_r \quad (\text{A17})$$

$$\partial_r (G_y^{\text{gravity}}) \approx \int \frac{2a}{r^3} (-\sin \phi T_\theta^t - \cot \theta \cos \phi T_\phi^t) dS_r \approx \int_\theta \int_\phi (|\boldsymbol{\Omega}_{\text{LT}}| L_{x,\text{total}}) dS_r \quad (\text{A18})$$

where the final step uses equations [A3](#) and [A16](#). Thus our identification recovers the LT torque to leading order. Moreover, combinations such as $\frac{\cos \phi}{\sin^2 \theta} T_\phi^\theta - \cos \phi T_\theta^\phi$, and $\frac{\sin \phi}{\sin^2 \theta} T_\phi^\theta - \sin \phi T_\theta^\phi$ vanish in Schwarzschild and appear only in rotating spacetimes, consistent with their interpretation as frame-dragging corrections.

Although the weak-field check supports our classification, there remains a possibility that some terms in our formulation are misclassified in the high-spin limit. We therefore compute Ω_{LT} to higher order using Kerr orbital frequencies ([Okazaki et al. 1987; Merloni et al. 1999](#))

$$\Omega_\phi = \pm \frac{1}{r^{3/2} \pm a}; \quad \Omega_\theta = \pm \left(\Omega_\phi^2 \left(1 \mp \frac{4a}{r^{3/2}} + \frac{3a^2}{r^2} \right) \right)^{1/2}; \quad \Omega_{LT} \equiv \Omega_\phi - \Omega_\theta, \quad (\text{A19})$$

where the upper/lower sign refers to prograde/retrograde spin. Figure [8](#) compares the resulting LT torque to our derived gravitational torque (averaged over the final $5000 r_g/c$) for high-spin prograde and retrograde runs. Agreement remains excellent for $r \gtrsim 5 r_g$, with small near-horizon deviations attributable to strong curvature.

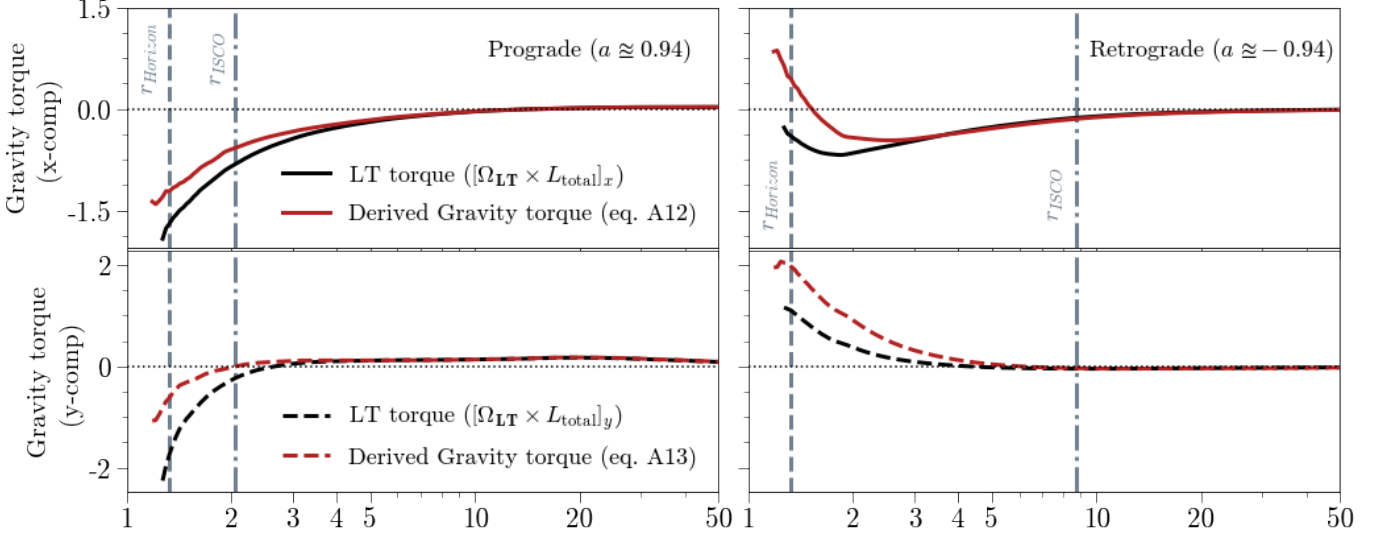


Figure 9. Radial profiles of the gravitational torque derived in Appendix A.2 (red; equations A12 and A13) compared to the LT torque (black) for high-spin prograde (left) and retrograde (right) runs. Curves are averaged over the final 5000 r_g/c . The agreement is excellent for $r \gtrsim 5 r_g$, with modest deviations at smaller radii where strong-field effects become important.

A.4. Torques in disk frame

Because the disk is tilted, alignment and precession are controlled by the components of the torque projected parallel and perpendicular to the *instantaneous* angular-momentum direction. To avoid geometric mixing of components in the simulation frame, we evaluate the local dynamics of each annulus in a disk-aligned coordinate system (r, θ', ϕ') obtained by a rotation that aligns \hat{z}' with the shell-integrated angular-momentum unit vector,

$$\hat{z}' \equiv \hat{t}(r, t), \quad \hat{t}(r, t) \equiv \frac{[\mathbf{L}_{\text{total}}]_{S_r}}{|\mathbf{L}_{\text{total}}|_{S_r}}. \quad (\text{A20})$$

We define the total twist (precession) angle as $\mathcal{P}(r, t) \equiv \tan^{-1} \left(\frac{[L_y]_{S_r}}{[L_x]_{S_r}} \right)$, and complete the orthonormal triad by choosing \hat{x}' to lie in the local averaged-disk plane and sets the zero of ϕ' ,

$$\hat{x}' \equiv \frac{\partial \hat{t}}{\partial \mathcal{I}_{+z}}, \quad \hat{y}' \equiv \hat{z}' \times \hat{x}' = \frac{1}{\sin \mathcal{I}_{+z}} \frac{\partial \hat{t}}{\partial \mathcal{P}}, \quad (\text{A21})$$

where $\mathcal{I}_{+z}(r, t)$ is the *instantaneous* tilt relative to the $+z$ axis of the simulation frame. The corresponding angular coordinates (θ', ϕ') are smooth functions of (θ, ϕ) and $(\mathcal{I}_{+z}, \mathcal{P})$; explicit expressions are given by White et al. (2019). On hypersurfaces of fixed r and t , this transformation is a local rotation, so $dr' = dr$ and the radial area element is invariant:

$$dS'_r \equiv \sqrt{-g'} d\theta' d\phi' = \sqrt{-g} d\theta d\phi \equiv dS_r, \quad (\text{A22})$$

with $g' \equiv \det(g_{\mu'\nu'})$ and $g_{\mu'\nu'} = \frac{\partial x^\alpha}{\partial x^{\mu'}} \frac{\partial x^\beta}{\partial x^{\nu'}} g_{\alpha\beta}$.

Since $\nabla_\mu T^\mu_\nu = 0$ is covariant, the energy-momentum conservation equations and the resulting angular-momentum balance relations have the same form in the disk frame as in the simulation frame after the replacement $(\theta, \phi) \rightarrow (\theta', \phi')$. For reproducibility, we write the full expressions below in a compact shorthand notation as:

$$\partial_r (G_{z'}) = \underbrace{-\partial_r \left(\int T_{\phi'}^r dS'_r \right)}_{\text{Matter + EM torque (z'-comp)}} , \quad (\text{A23})$$

$$\partial_r (G_{x'}) = \underbrace{\partial_r \left(\int (\sin \phi' T_{\theta'}^r + \cot \theta' \cos \phi' T_{\phi'}^r) dS'_r \right)}_{\text{Matter + EM torque (}x'\text{-comp)}} + \underbrace{\int \left(-\sin \phi' T_{\lambda'}^{\kappa'} \Gamma_{\theta' \kappa'}^{\lambda'} + \cot \theta' \sin \phi' T_{\phi'}^{\theta'} + \frac{\cos \phi'}{\sin^2 \theta'} T_{\phi'}^{\theta'} - \cos \phi' T_{\theta'}^{\phi'} \right) dS'_r}_{\text{Gravitational torque (}x'\text{-comp)}} \quad (\text{A24})$$

$$\partial_r (G_{y'}) = \underbrace{\partial_r \left(\int (-\cos \phi' T_{\theta'}^r + \cot \theta' \sin \phi' T_{\phi'}^r) dS'_r \right)}_{\text{Matter + EM torque (}y'\text{-comp)}} + \underbrace{\int \left(\cos \phi' T_{\lambda'}^{\kappa'} \Gamma_{\theta' \kappa'}^{\lambda'} - \cot \theta' \cos \phi' T_{\phi'}^{\theta'} + \frac{\sin \phi'}{\sin^2 \theta'} T_{\phi'}^{\theta'} - \sin \phi' T_{\theta'}^{\phi'} \right) dS'_r}_{\text{Gravitational torque (}y'\text{-comp)}} \quad (\text{A25})$$

where $T_{\nu'}^{\mu'}$, $\Gamma_{\theta' \kappa'}^{\lambda'}$ are the stress-energy and connection coefficient components in the disk-aligned frame. It is important to note that the Christoffel connection does not transform as a tensor. Physically, this transformation “unwarps” each spherical shell by rotating into the local disk orientation. In this frame the torque components have a direct kinematic interpretation: $G_{x'}$ and $G_{y'}$ control changes in the annulus orientation (tilt and twist) with a subtle difference that we describe later, while $G_{z'}$ changes the shell-integrated angular-momentum magnitude and describes accretion torque (Balbus & Hawley 1998).

Because we diagnose tilt and twist for a *single annulus*, we work with shell-integrated angular-momentum components whose evolution is set by radial fluxes determined by radial torque gradients (Sorathia et al. (2013), equations A11, A12 and A13). This “per-shell” viewpoint introduces an additional, purely geometric contribution when determining the rate of change of tilt and twist: the local disk basis varies with radius, so projections change both because the torque changes and because basis rotate across the shell. Using equation A2 (and $\mathcal{I}_{+z} = \mathcal{I}_{\text{BH}}$ for prograde, $\mathcal{I}_{+z} = \pi - \mathcal{I}_{\text{BH}}$ for retrograde), the simulation-frame expression is

$$\partial_t (\mathcal{I}_{+z}) = \frac{1}{|[\mathbf{L}]_{S_r}|} (\cos \mathcal{I}_{+z} \cos \mathcal{P} \partial_r (G_x^{\text{total}}) + \cos \mathcal{I}_{+z} \sin \mathcal{P} \partial_r (G_y^{\text{total}}) - \sin \mathcal{I}_{+z} \partial_r (G_z^{\text{total}})) \quad (\text{A26})$$

In the disk frame the evolution separates cleanly into torque-gradient and geometric (shear-coupling) terms:

$$\partial_t (\mathcal{I}_{+z}) = \frac{1}{|[\mathbf{L}]_{S_r}|} (\partial_r (G_{x'}^{\text{total}}) - \mathcal{S}_{x'}) \quad (\text{A27})$$

$$\partial_t (\mathcal{P}) = \frac{1}{|[\mathbf{L}]_{S_r}| \sin \mathcal{I}_{+z}} (\partial_r (G_{y'}^{\text{total}}) - \mathcal{S}_{y'}) \quad (\text{A28})$$

where $\mathcal{S}_{x'}$, $\mathcal{S}_{y'}$ are shear-coupling terms arise from radial variation of the local basis vectors. These equations are similar to Philippov et al. (2014) with the only difference of additional shear-coupling terms. Projecting the simulation-frame (matter+EM) torque components into the disk frame and differentiating the basis vector gives:

$$\mathcal{S}_{x'} \equiv \left[\mathbf{G}'^{\text{MA+EM}} \cdot \partial_r (\hat{\mathbf{x}}') \right] = -G_{z'} \frac{\partial (\mathcal{I}_{+z})}{\partial r} + G_{y'}^{\text{MA+EM}} \cos \mathcal{I}_{+z} \frac{\partial \mathcal{P}}{\partial r} \quad (\text{A29})$$

$$\mathcal{S}_{y'} \equiv \left[\mathbf{G}'^{\text{MA+EM}} \cdot \partial_r (\hat{\mathbf{y}}') \right] = -\frac{\partial \mathcal{P}}{\partial r} (\sin \mathcal{I}_{+z} G_{z'} + \cos \mathcal{I}_{+z} G_{x'}^{\text{MA+EM}}) \quad (\text{A30})$$

with “MA+EM” denoting the matter and EM torques from equations A24 and A25. The above shear terms (i) vanish for a locally rigid annulus ($\partial_r (\mathcal{I}_{+z}) = \partial_r (\mathcal{P}) = 0$), (ii) are independent of coordinate gauge because they are inner products; and (iii) do not represent a new physical torque channel. Rather, they are connection-like terms that encode the coupling between the physical torque and the radially rotating, non-inertial disk frame (analogous to Coriolis-type terms in rotating coordinates).

Finally, to leading order in a/r we estimate the gravitational torque in the disk frame by projecting the LT angular velocity onto the local basis,

$$\boldsymbol{\Omega}'_{LT}(r, t) = (-\Omega_{LT} \sin \mathcal{I}, 0, \Omega_{LT} \cos \mathcal{I}). \quad (\text{A31})$$

so that the per-shell torque satisfies

$$\partial_r(\mathbf{G}'_{\text{gravity}}) \approx \boldsymbol{\Omega}'_{LT} \times (|\mathbf{L}|_{S_r} \hat{\mathbf{z}}') \quad (\text{A32})$$

implying

$$\partial_r(G_{x'}^{\text{gravity}}) \simeq 0, \quad \partial_r(G_{y'}^{\text{gravity}}) \simeq \Omega_{LT} |\mathbf{L}|_{S_r} \sin \mathcal{I}_{+z}, \quad \partial_r(G_{z'}^{\text{gravity}}) \simeq 0 \quad (r \gg a). \quad (\text{A33})$$

As expected, the LT torque is perpendicular to \mathbf{L} and therefore drives precession without changing $|\mathbf{L}|_{S_r}$ or \mathcal{I}_{+z} . Since $\sin \mathcal{I}_{+z} > 0$ and Ω_{LT} has the sign of the BH spin (positive for prograde, negative for retrograde), LT precession is always in the sense set by the spin

B. MEASUREMENT OF THE JET INCLINATION

We measured jet inclination using the method of [Liska et al. \(2018\)](#), with one modification: we identify the jet by magnetization, $\sigma \equiv b^2/(2\rho) > 1$, rather than their criterion $p_{\text{mag}}/\rho > 1/(2r)$. The two prescriptions agree within $\sim 50 r_g$, but at larger radii the [Liska et al. \(2018\)](#) criterion aligned more closely with the disk due to increased mass loading. For $r > 10 r_g$ we separate the jet into upper ($0 < \theta < \pi/2$) and lower ($\pi/2 < \theta < \pi$) hemispheres. For $r \leq 10 r_g$, where the tilted disk complicates a hemispheric split, we instead use the sign of the radial magnetic field: upper ($b^r > 0$) and lower ($b^r < 0$). At each (r, t) we compute magnetic-pressure-weighted centroids of the upper and lower regions in Cartesian coordinates and define the local jet axis from the centroid separation; the reported jet inclination is obtained by averaging this axis over radius.

C. SYMMETRY AND TILT CONSISTENCY IN PROGRADE AND RETROGRADE MADS

Because only the *relative* orientation between the BH spin and disk angular momentum is physical, a prograde/retrograde setup can be implemented either by rotating the torus at fixed spin or by reversing the spin at fixed torus orientation. To verify that this symmetry does not bias the MAD state or the tilt evolution, we performed two additional runs. For the physically prograde configuration we set $a = -0.9375$ and rotate the torus angular momentum by 164° about the y -axis, giving an effective misalignment of 16° between the BH spin and disk. For the physically retrograde configuration we set $a = +0.9375$ with the same 164° torus rotation, giving a misalignment of 164° . Both runs use resolution $160 \times 128 \times 80$ in (r, θ, ϕ) , and disk tilt is computed using equation 10.

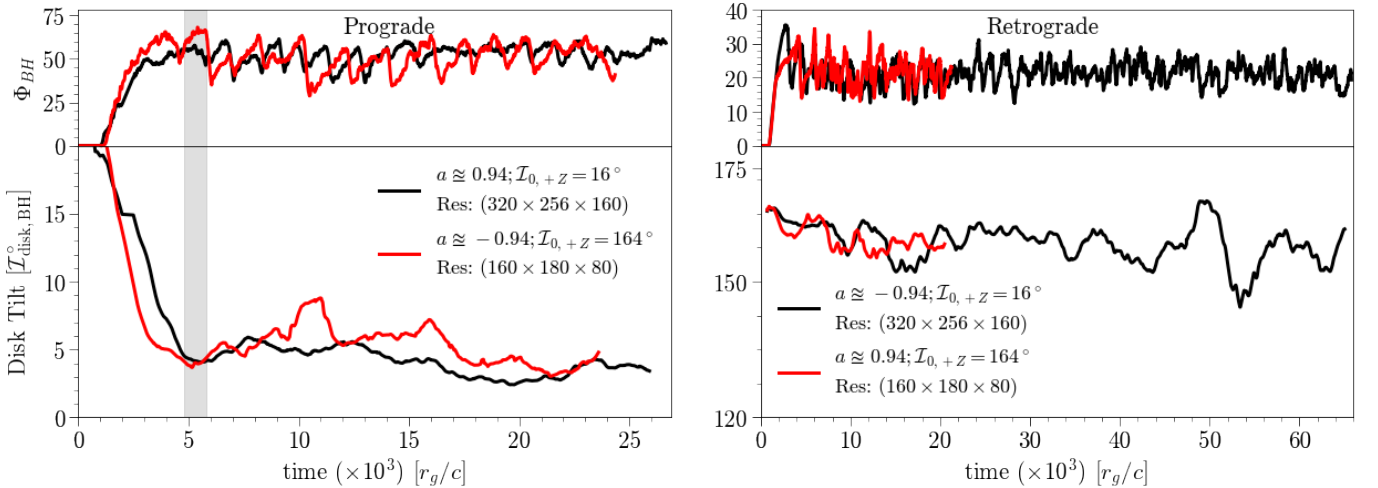


Figure 10. Test of the setup symmetry between BH-spin sign and initial torus rotation. Curves compare the horizon magnetic-flux and the inner-disk tilt (measured out to $20 r_g$ using equation 10) between physically equivalent realizations of prograde (left column) and retrograde (right column) configurations. Black curves show the reference high-spin runs ($a \simeq 0.94$, $\mathcal{I}_{0,+z} = 16^\circ$ for prograde; $a \simeq -0.94$, $\mathcal{I}_{0,+z} = 16^\circ$ for retrograde), while red curves show the alternative implementations obtained by flipping the spin sign and adjusting the torus rotation. The MAD saturation and tilt evolution agree closely, indicating that the results are insensitive to this setup convention (and remain consistent when the resolution is reduced by a factor of eight).

Figure 10 shows that both the MAD level and the inner ($\leq 20 r_g$) tilt evolution are consistent between symmetry-related setups for the prograde and retrograde cases. Although reversing the spin sign changes the ISCO in HARMPI

and can modify near-horizon dynamics, the tilt evolution exhibits similar trends and magnitudes across configurations, indicating that the tilt dynamics are robust to this setup choice.

REFERENCES

Abramowicz, M. A., Calvani, M., & Nobili, L. 1980, ApJ, 242, 772, doi: [10.1086/158512](https://doi.org/10.1086/158512)

Adler, R., Bazin, M., & Schiffer, M. 1965, Introduction to General Relativity, International series in pure and applied physics (McGraw-Hill).
<https://books.google.com/books?id=vHUuAAAAIAAJ>

Balbus, S. A., & Hawley, J. F. 1998, Reviews of Modern Physics, 70, 1, doi: [10.1103/RevModPhys.70.1](https://doi.org/10.1103/RevModPhys.70.1)

Bardeen, J. M. 1970, Nature, 226, 64, doi: [10.1038/226064a0](https://doi.org/10.1038/226064a0)

Bardeen, J. M., & Petterson, J. A. 1975, ApJL, 195, L65, doi: [10.1086/181711](https://doi.org/10.1086/181711)

Begelman, M. C., Scepi, N., & Dexter, J. 2022, Monthly Notices of the Royal Astronomical Society, 511, 2040, doi: [10.1093/mnras/stab3790](https://doi.org/10.1093/mnras/stab3790)

Blandford, R. D., & Payne, D. G. 1982, MNRAS, 199, 883, doi: [10.1093/mnras/199.4.883](https://doi.org/10.1093/mnras/199.4.883)

Blandford, R. D., & Znajek, R. L. 1977, Monthly Notices of the Royal Astronomical Society, 179, 433, doi: [10.1093/mnras/179.3.433](https://doi.org/10.1093/mnras/179.3.433)

Carroll, S. 2003, Spacetime and Geometry: An Introduction to General Relativity (Benjamin Cummings).
<http://www.amazon.com/Spacetime-Geometry-Introduction-General-Relativity/dp/0805387323>

Chatterjee, K., Kaaz, N., Liska, M., Tchekhovskoy, A., & Markoff, S. 2025, Phys. Rev. D, 112, 063013, doi: [10.1103/hgj9-v4fk](https://doi.org/10.1103/hgj9-v4fk)

Chatterjee, K., Younsi, Z., Liska, M., et al. 2020, Monthly Notices of the Royal Astronomical Society, 499, 362, doi: [10.1093/mnras/staa2718](https://doi.org/10.1093/mnras/staa2718)

Collaboration, E. H. T., Akiyama, K., Alberdi, A., et al. 2022, The Astrophysical Journal Letters, 930, L16, doi: [10.3847/2041-8213/ac6672](https://doi.org/10.3847/2041-8213/ac6672)

Collaboration, T. E. H. T., Akiyama, K., Algaba, J. C., et al. 2021, The Astrophysical Journal Letters, 910, L13, doi: [10.3847/2041-8213/abe4de](https://doi.org/10.3847/2041-8213/abe4de)

Dexter, J., Jiménez-Rosales, A., Ressler, S. M., et al. 2020, Monthly Notices of the Royal Astronomical Society, 494, 4168, doi: [10.1093/mnras/staa922](https://doi.org/10.1093/mnras/staa922)

E., B. 2000, Introduction to tensor calculus for general relativity, lecture notes edn. (MIT).
<http://gen.lib.rus.ec/book/index.php?md5=57b0fc8a8d0ed572de3f7e7885714e0e>

Fishbone, L. G., & Moncrief, V. 1976, ApJ, 207, 962, doi: [10.1086/154565](https://doi.org/10.1086/154565)

Font, J. A., Ibáñez, J. M., & Papadopoulos, P. 1998, The Astrophysical Journal, 507, L67, doi: [10.1086/311666](https://doi.org/10.1086/311666)

Fragile, P. C., Blaes, O. M., Anninos, P., & Salmonson, J. D. 2007, The Astrophysical Journal, 668, 417, doi: [10.1086/521092](https://doi.org/10.1086/521092)

Gammie, C. F., McKinney, J. C., & Toth, G. 2003, The Astrophysical Journal, 589, 444, doi: [10.1086/374594](https://doi.org/10.1086/374594)

Genzel, R., Eisenhauer, F., & Gillessen, S. 2010, Rev. Mod. Phys., 82, 3121, doi: [10.1103/RevModPhys.82.3121](https://doi.org/10.1103/RevModPhys.82.3121)

Ghez, A. M., Klein, B. L., Morris, M., & Becklin, E. E. 1998, ApJ, 509, 678, doi: [10.1086/306528](https://doi.org/10.1086/306528)

Gupta, S., & Dexter, J. 2024, The Astrophysical Journal, 974, 209, doi: [10.3847/1538-4357/ad737d](https://doi.org/10.3847/1538-4357/ad737d)

Harris, C. R., Millman, K. J., van der Walt, S. J., et al. 2020, Nature, 585, 357, doi: [10.1038/s41586-020-2649-2](https://doi.org/10.1038/s41586-020-2649-2)

Hunter, J. D. 2007, Computing in Science & Engineering, 9, 90, doi: [10.1109/MCSE.2007.55](https://doi.org/10.1109/MCSE.2007.55)

Igumenshchev, I. V. 2008, The Astrophysical Journal, 677, 317, doi: [10.1086/529025](https://doi.org/10.1086/529025)

Igumenshchev, I. V., Narayan, R., & Abramowicz, M. A. 2003, ApJ, 592, 1042, doi: [10.1086/375769](https://doi.org/10.1086/375769)

Ingram, A., van der Klis, M., Middleton, M., et al. 2016, Monthly Notices of the Royal Astronomical Society, 461, 1967, doi: [10.1093/mnras/stw1245](https://doi.org/10.1093/mnras/stw1245)

Ivanov, P. B., & Illarionov, A. F. 1997, MNRAS, 285, 394, doi: [10.1093/mnras/285.2.394](https://doi.org/10.1093/mnras/285.2.394)

Jiang, H.-X., Mizuno, Y., Lai, D., Dihingia, I. K., & Fromm, C. M. 2025, The Astrophysical Journal, 995, 112, doi: [10.3847/1538-4357/ae19ee](https://doi.org/10.3847/1538-4357/ae19ee)

Jiang, Y.-F., Stone, J. M., & Davis, S. W. 2019, The Astrophysical Journal, 880, 67, doi: [10.3847/1538-4357/ab29ff](https://doi.org/10.3847/1538-4357/ab29ff)

Katz, J. 1980, Astrophysical Journal, Part 2-Letters to the Editor, vol. 236, Mar. 15, 1980, p. L127-L130., 236, L127

King, A. R., Lubow, S. H., Ogilvie, G. I., & Pringle, J. E. 2005, Monthly Notices of the Royal Astronomical Society, 363, 49, doi: [10.1111/j.1365-2966.2005.09378.x](https://doi.org/10.1111/j.1365-2966.2005.09378.x)

Larwood, J. 1998, Monthly Notices of the Royal Astronomical Society, 299, L32, doi: [10.1046/j.1365-8711.1998.01978.x](https://doi.org/10.1046/j.1365-8711.1998.01978.x)

Lense, J., & Thirring, H. 1918, Physikalische Zeitschrift, 19, 156

Liska, M., Hesp, C., Tchekhovskoy, A., et al. 2018, *MNRAS*, 474, L81, doi: [10.1093/mnrasl/slx174](https://doi.org/10.1093/mnrasl/slx174)

Liska, M., Tchekhovskoy, A., Ingram, A., & van der Klis, M. 2019, *Monthly Notices of the Royal Astronomical Society*, 487, 550, doi: [10.1093/mnras/stz834](https://doi.org/10.1093/mnras/stz834)

Lubow, S. H., Ogilvie, G. I., & Pringle, J. E. 2002, *Monthly Notices of the Royal Astronomical Society*, 337, 706, doi: [10.1046/j.1365-8711.2002.05949.x](https://doi.org/10.1046/j.1365-8711.2002.05949.x)

McKinney, J. C., Tchekhovskoy, A., & Blandford, R. D. 2012, *MNRAS*, 423, 3083, doi: [10.1111/j.1365-2966.2012.21074.x](https://doi.org/10.1111/j.1365-2966.2012.21074.x)

McKinney, J. C., Tchekhovskoy, A., & Blandford, R. D. 2013, *Science*, 339, 49, doi: [10.1126/science.1230811](https://doi.org/10.1126/science.1230811)

Merloni, A., Vietri, M., Stella, L., & Bini, D. 1999, *MNRAS*, 304, 155, doi: [10.1046/j.1365-8711.1999.02307.x](https://doi.org/10.1046/j.1365-8711.1999.02307.x)

Mewes, V., Font, J. A., Galeazzi, F., Montero, P. J., & Stergioulas, N. 2016, *Physical Review D*, 93, 064055

Misner, C., Thorne, K., & Wheeler, J. 1973, *Gravitation* (W. Freeman)

Narayan, R., Chael, A., Chatterjee, K., Ricarte, A., & Curd, B. 2022, *Monthly Notices of the Royal Astronomical Society*, 511, 3795, doi: [10.1093/mnras/stac285](https://doi.org/10.1093/mnras/stac285)

Narayan, R., Igumenshchev, I. V., & Abramowicz, M. A. 2003, *Publications of the Astronomical Society of Japan*, 55, L69, doi: [10.1093/pasj/55.6.L69](https://doi.org/10.1093/pasj/55.6.L69)

Narayan, R., Sadowski, A., Penna, R. F., & Kulkarni, A. K. 2012, *MNRAS*, 426, 3241, doi: [10.1111/j.1365-2966.2012.22002.x](https://doi.org/10.1111/j.1365-2966.2012.22002.x)

Nelson, R. P., & Papaloizou, J. C. B. 2000, *Monthly Notices of the Royal Astronomical Society*, 315, 570, doi: [10.1046/j.1365-8711.2000.03478.x](https://doi.org/10.1046/j.1365-8711.2000.03478.x)

Nixon, C., King, A., & Price, D. 2013, *Monthly Notices of the Royal Astronomical Society*, 434, 1946, doi: [10.1093/mnras/stt1136](https://doi.org/10.1093/mnras/stt1136)

Nixon, C. J., & King, A. R. 2012, *Monthly Notices of the Royal Astronomical Society*, 421, 1201, doi: [10.1111/j.1365-2966.2011.20377.x](https://doi.org/10.1111/j.1365-2966.2011.20377.x)

Noble, S. C., Gammie, C. F., McKinney, J. C., & Zanna, L. D. 2006, *The Astrophysical Journal*, 641, 626, doi: [10.1086/500349](https://doi.org/10.1086/500349)

Okazaki, A. T., Kato, S., & Fukue, J. 1987, *PASJ*, 39, 457

Papaloizou, J. C. B., & Lin, D. N. C. 1995, *ApJ*, 438, 841, doi: [10.1086/175127](https://doi.org/10.1086/175127)

Penna, R. F., McKinney, J. C., Narayan, R., et al. 2010, *Monthly Notices of the Royal Astronomical Society*, 408, 752, doi: [10.1111/j.1365-2966.2010.17170.x](https://doi.org/10.1111/j.1365-2966.2010.17170.x)

Philippov, A., Tchekhovskoy, A., & Li, J. G. 2014, *Monthly Notices of the Royal Astronomical Society*, 441, 1879, doi: [10.1093/mnras/stu591](https://doi.org/10.1093/mnras/stu591)

Polko, P., & McKinney, J. C. 2016, *Monthly Notices of the Royal Astronomical Society*, 464, 2660, doi: [10.1093/mnras/stw1875](https://doi.org/10.1093/mnras/stw1875)

Pringle, J. E. 1997, *Monthly Notices of the Royal Astronomical Society*, 292, 136, doi: [10.1093/mnras/292.1.136](https://doi.org/10.1093/mnras/292.1.136)

Raj, A., Nixon, C. J., & Doğan, S. 2021, *The Astrophysical Journal*, 909, 81, doi: [10.3847/1538-4357/abdc24](https://doi.org/10.3847/1538-4357/abdc24)

Ressler, S. M., Tchekhovskoy, A., Quataert, E., & Gammie, C. F. 2017, *MNRAS*, 467, 3604, doi: [10.1093/mnras/stx364](https://doi.org/10.1093/mnras/stx364)

Scepi, N., Begelman, M. C., & Dexter, J. 2023, *Monthly Notices of the Royal Astronomical Society*, 527, 1424, doi: [10.1093/mnras/stad3299](https://doi.org/10.1093/mnras/stad3299)

Schandl, S., & Meyer, F. 1994, *A&A*, 289, 149

Sorathia, K. A., Krolik, J. H., & Hawley, J. F. 2013, *The Astrophysical Journal*, 777, 21, doi: [10.1088/0004-637x/777/1/21](https://doi.org/10.1088/0004-637x/777/1/21)

Tchekhovskoy, A. 2019, *Astrophysics Source Code Library*, ascl

Tchekhovskoy, A., Narayan, R., & McKinney, J. C. 2010, *The Astrophysical Journal*, 711, 50, doi: [10.1088/0004-637X/711/1/50](https://doi.org/10.1088/0004-637X/711/1/50)

—. 2011, *Monthly Notices of the Royal Astronomical Society: Letters*, 418, L79, doi: [10.1111/j.1745-3933.2011.01147.x](https://doi.org/10.1111/j.1745-3933.2011.01147.x)

White, C. J., Quataert, E., & Blaes, O. 2019, *The Astrophysical Journal*, 878, 51, doi: [10.3847/1538-4357/ab089e](https://doi.org/10.3847/1538-4357/ab089e)

White, C. J., Quataert, E., & Gammie, C. F. 2020, *The Astrophysical Journal*, 891, 63, doi: [10.3847/1538-4357/ab718e](https://doi.org/10.3847/1538-4357/ab718e)

Wijers, R. A. M. J., & Pringle, J. E. 1999, *Monthly Notices of the Royal Astronomical Society*, 308, 207, doi: [10.1046/j.1365-8711.1999.02720.x](https://doi.org/10.1046/j.1365-8711.1999.02720.x)

You, B., Cao, X., Yan, Z., et al. 2023, *Science*, 381, 961, doi: [10.1126/science.abo4504](https://doi.org/10.1126/science.abo4504)

Yuan, F., Quataert, E., & Narayan, R. 2003, *The Astrophysical Journal*, 598, 301, doi: [10.1086/378716](https://doi.org/10.1086/378716)

Yuan, F., Wang, H., & Yang, H. 2022, *The Astrophysical Journal*, 924, 124, doi: [10.3847/1538-4357/ac4714](https://doi.org/10.3847/1538-4357/ac4714)